J. Fluid Mech. (1996), *vol.* 315, *pp.* 175–221

Vortical structure morphology in the initial region of a forced mixing layer: roll-up and pairing

By RICHARD L. LEBOEUF[1] AND RABINDRA D. MEHTA[2]

[1]Center for Turbulence Research, NASA Ames Research Center/Stanford University, Stanford, CA 94305, USA.

[2]Department of Aeronautics and Astronautics, JIAA, Stanford University, Stanford *and* Fluid Mechanics Laboratory, NASA Ames Research Center, Moffett Field, CA 94035-1000, USA

(Received 7 July 1994 and in revised form 5 January 1996)

Detailed three-dimensional phase-averaged measurements of the spanwise and streamwise vorticity formation and evolution in a forced mixing layer have been obtained. A plane two-stream mixing layer with a velocity ratio (U_2/U_1) of 0.6, a maximum Reynolds number (Re_δ) of about 3150 and laminar initial boundary layers was generated in a mixing layer wind tunnel. Acoustic forcing, consisting of a fundamental roll-up frequency and its subharmonic, was used to phase-lock the initial development and first pairing of the spanwise vortical structures. For the first time, phase-averaged measurements of all three velocity components have been obtained on a three-dimensional grid, yielding the spanwise and streamwise vorticity distributions without invoking Taylor's hypothesis. The phase-averaged results show that the streamwise vorticity first appears in the form of 'ribs' just upstream of the first spanwise vortex roll-up. At the same time, the first spanwise roller becomes kinked, thus also contributing to the streamwise vorticity. As a result, in cross-stream cuts through the spanwise rollers, the streamwise vorticity appears in a 'three-tier' arrangement with opposite-signed vorticity in the centre. In terms of phase-averaged quantities, the maximum streamwise vorticity in the initial ribs is equivalent to about 10–15% of the peak spanwise vorticity and the streamwise rib circulation is equivalent to about 5–10% of the spanwise circulation. Further downstream, the peak streamwise vorticity decreases with increasing distance, while the average circulation remains approximately constant. Downstream of the pairing, the streamwise vorticity levels in the spanwise rollers are reduced. However, the spanwise spacing of the streamwise vortices does *not* increase within the measurement domain. Phase-averaged Reynolds stress measurements show that relatively high stress levels (periodic and random) were generated in the cores of the spanwise vortices.

1. Introduction

The mixing layer, being one of the fundamental transitional flows as well as a technologically significant turbulent flow, has been scrutinized for many decades, both experimentally and computationally (Ho & Huerre 1984). Many of the earlier experimental investigations involved flow visualization studies and one-dimensional (single-profile) measurements of mean velocity and time-averaged turbulence quanti-

ties. The results of these studies were useful in assessing qualitative structural features and also for corroborating turbulence theories and tuning turbulence models.

In the early seventies, a better understanding of the mixing layer structure was gleaned from results of more detailed investigations (Brown & Roshko 1974; Winant & Browand 1974). These studies revealed that well-organized spanwise vortical structures ('rollers') were generated as a result of the Kelvin–Helmholtz instability and that their pairing was a controlling factor for mixing layer growth. In addition to the spanwise coherent structures, a secondary structure, in the form of spatially stationary streamwise vortices, was also soon identified in flow visualization studies of plane mixing layers (Konrad 1976; Breidenthal 1981; Bernal & Roshko 1986; Lasheras, Cho & Maxworthy 1986). These results showed that the streamwise structures first formed in the *braid* region, a region connecting adjacent spanwise vortices which lacks significant spanwise vorticity and is dominated by the large-scale strain rate. The extensional principal axis of the strain rate field in the braid region lies in a vertical (X, Y) plane, but at an angle to the streamwise direction. These earlier results also showed that the locations of the streamwise vortical structures were related to the strength and position of (weak) incoming disturbances. Models of the three-dimensional mixing layer structure soon emerged which showed an inclined vortex tube structure in the braid region which wound back and forth between adjacent spanwise rollers (Bernal & Roshko 1986; Lasheras *et al.* 1986). Attempts to quantify observations regarding the three-dimensional structure quickly followed (Jimenez 1983; Jimenez, Cogollos & Bernal 1985; Huang & Ho 1990). These results confirmed earlier observations that the streamwise structures were indeed spatially stationary. Some evidence of their scale, and hence spacing, increasing with downstream distance was also reported. A detailed review of the work on spanwise scale change is given in Leboeuf & Mehta (1995*a*).

The presence and role of these 'naturally occurring' streamwise structures were investigated through detailed time-averaged measurements by Bell & Mehta (1992). A plane, two-stream mixing layer was generated, with a velocity ratio of 0.6, and laminar initial boundary layers which were nominally two-dimensional. The measurements indicated that small spanwise disturbances originating upstream in the boundary layer flow were amplified, leading to the formation of spatially stationary streamwise vortices. Based on mean velocity measurements in the near-field region, it was concluded that this amplification occurred just downstream of the first spanwise vortex roll-up. The mean vorticity first appeared in 'clusters' containing vorticity of both signs, but further downstream, it ' re-aligned' to form counter-rotating pairs in a nominally linear arrangement. Unfortunately, the mechanism for this rearrangement could not be inferred from the time-averaged measurements. The vortex structure was found to grow in size with downstream distance, the spanwise wavelength associated with them increasing in a stepwise fashion and scaling approximately with the local mixing layer vorticity thickness. These vortical structures also weakened downstream, the maximum mean streamwise vorticity decaying as approximately $1/X^{1.5}$. Using two-point cross-correlation measurements, LeBoeuf & Mehta (1993) showed that this decay is most likely due to actual weakening of the instantaneous streamwise vorticity rather than an artifact of meander.

Secondary structure eduction aided by artificial (two-dimensional) excitation of the mixing layer roll-up and pairing has also been attempted in some studies. Huang & Ho (1990) measured the 'partial streamwise vorticity' $(\partial V/\partial Z)$ in a forced mixing layer and found that the spanwise spacing of the streamwise structures doubled after each of the first two pairings of the spanwise rollers. They also concluded

that the secondary vortices developed at the same time that the spanwise structures were formed. Nygaard & Glezer (1990, 1991) excited spanwise-periodic streamwise vortices using a time-harmonic waveform synthesized by a mosaic of surface film heaters. By reconstructing the streamwise development of a partial vorticity using Taylor's hypothesis, they observed that the streamwise vortices formed upstream of the first spanwise roll-up. Further downstream, the streamwise vortices essentially resided in the braid region. They also found that almost any imposed wavelength would lead to the generation of the streamwise structures. If the spanwise excitation wavelength exceeded the initial Kelvin–Helmholtz wavelength, the primary vortices developed spanwise undulations associated with the 'core' instability first proposed by Pierrehumbert & Widnall (1982). Tung (1992) measured all three velocity components in a forced mixing layer and also used Taylor's hypothesis to transform the (phase-averaged) temporal measurements onto a 'spatial' domain. Tung first observed concentrated streamwise vortices at the start of the first spanwise structure pairing, and these, together with additional generated vortices, soon formed the familiar single row of counter-rotating pairs. Toward completion of the spanwise vortex merging, he also observed a pairing between streamwise vortices of the same sign, as had been previously hypothesized by Bell & Mehta (1992) and has been recently observed in a forced mixing layer by LeBoeuf & Mehta (1995*a*). However, a global doubling of the spanwise wavelength was not observed downstream of the roller pairing.

There are also many computational studies of mixing layer development. For mixing layer computations, disturbances have to be introduced in order to trigger instability mechanisms. Consequently, several early computational studies were used to examine the effects of two-dimensional single- and multiple-frequency forcing on roll-up and merging of the primary rollers. Using a numerical solution to two-dimensional Boussinesq equations, Patnaik, Sherman & Corcos (1976) showed that the combined effect of fundamental and subharmonic forcing was a function of the relative forcing signal phases. In particular, with the fundamental and subharmonic in phase, adjacent spanwise rollers merge via a 'shredding interaction', and with the fundamental and subharmonic out of phase, adjacent spanwise rollers merge via a 'rolling interaction'. These results were later confirmed by several investigators: Riley & Metcalfe (1980) using two- and three-dimensional temporal simulations, Monkewitz (1988) using an instability-wave analysis, and Inoue (1992) using a spatial simulation employing a two-dimensional vortex tracking method. Inoue (1992) also examined the effects of other combinations of forcing signal frequencies which resulted in a variety of pairing mechanisms including 'tripling', whereby the roller formed by amalgamation of two of every three first-generation primary rollers merges with the remaining first-generation roller. Several of these different pairing mechanisms including 'rolling', 'shredding' and 'tripling' had been previously identified in shadowgraph ciné films of an unforced mixing layer (Hernan & Jimenez 1982).

In addition to the two-dimensional simulations, which focused on the initial roll-up and pairing of the primary structure, several extensive three-dimensional computations have ellucidated the development and role of the streamwise vortices in the mixing layer structure morphology and evolution. The first of these simulations was reported by Inoue (1987) and Metcalfe *et al.* (1987). Inoue introduced small-amplitude three-dimensional disturbances into an otherwise two-dimensional spatially developing flow field generated using the vortex tracking method. The results showed that pairs of counter-rotating streamwise vortices would develop as a result of stretching of the primary roller. Metcalfe *et al.* (1987) studied the three-dimensional stability of two-dimensional vortical states of planar mixing layers using a temporal direct numerical

simulation. Their analysis confirmed the existence of counter-rotating streamwise vortices connecting the primary spanwise rollers. The coherence of these rib-like structures was found to depend strongly on the presence of the two-dimensional pairing modes. In particular, it was found that persistent pairings can inhibit the three-dimensional instability while suppression of the pairing process drove the three-dimensional modes to more chaotic, turbulent-like states.

Ashurst & Meiburg (1988) numerically simulated a temporally growing plane shear layer using the discrete vortex dynamics method. They showed that concentrated streamwise vortices formed in the braid region, whereas the spanwise core instability was observed to grow only initially. In contrast to these earlier studies, Buell & Mansour (1989) and Buell (1991) reported the direct numerical simulation of a spatially developing, three-dimensional mixing layer. In the simulation, a pair of counter-rotating streamwise vortices was added to an otherwise two-dimensional flow which was forced to roll up and pair. It was found that the local strain rate of the ribs caused the primary rollers to distort and generate 'cups' of spanwise vorticity at the bends of the rollers. Furthermore, kinking of the spanwise rollers in the streamwise direction introduced a streamwise vorticity component at the roller core with opposite sign to that of the surrounding rib vortices. They found that there was little direct effect of the pairing on the surviving ribs but conjectured that the imposition of different inflow boundary conditions may produce qualitatively different flows.

Spatial simulations soon gave way to the more economical large-eddy and direct numerical simulations of temporally evolving mixing layers. In a large-eddy simulation of a moderate to high Reynolds number turbulent mixing layer, Miyauchi, Kawano & Shingou (1991) found that the three-dimensional rib structures became well organized in spite of initial random fluctuations. It was noted that although 'tearing' of the primary structure was occurring in the high Reynolds number case, the rib structure was still identifiable. More recently, the most extensive set of direct numerical simulations of temporally evolving mixing layers has been reported by Rogers & Moser (1992, 1993) and Moser & Rogers (1993). These simulations have yielded complete details of the mixing layer structure and dynamics, starting from the formation of the initial spanwise vortex roll-up leading into the evolution of the mixing layer up to the third pairing.

In their initial simulations, Rogers & Moser (1992) investigated the Kelvin–Helmholtz roll-up using a few low-wavenumber disturbances in addition to the mean velocity profile. For most of their initial conditions, the spanwise vorticity rolled up into corrugated spanwise rollers resulting in strong cup-shaped regions of spanwise vorticity at the bend of the rollers and opposite-sign streamwise vorticity in the primary roller core, in agreement with the spatial simulation results (Buell & Mansour 1989; Buell 1991). Moser & Rogers (1993) extended the simulations to include up to the third pairing of the primary rollers. They showed that pairing in a significantly three-dimensional layer, containing cups and collapsed ribs, leads to a disorganization of the structures which is further complicated by vortex stretching. Newly created vortices and the remnants of the original rib vortices generate thin vortex sheets which undergo secondary roll-ups, thus generating smaller scales. A further pairing of this transitional flow results in a mixing layer which bears similarities to experimental turbulent mixing layers and the 'self-similar' layers recently simulated by Rogers & Moser (1994).

Rogers & Moser (1993) also examined their multiple-pairing mixing layers for evidence of spanwise scale changes. For initially infinitesimal disturbance levels, they found that three or more primary roller pairings were required to complete a

doubling of the spanwise scale. Stronger three-dimensionality produced more rapid scale changes, but it also led to early transition. Depending on the amplitude of the disturbances, the spanwise scale was found to double (or even quadruple) after zero, one or two pairings. These simulation results therefore suggest that the details of the spanwise scale change are dependent on the details of the disturbance environment, thereby making the whole process 'facility dependent'. Two mechanisms (viscous amalgamation and annihilation) were also identified by which an array of counter-rotating rib vortices may reorganize resulting in an increase in the spanwise length scale. Of course, these temporally developing, space-periodic mixing layers do not represent all the features of spatially developing mixing layers investigated in wind tunnels.

Although the secondary structure in a plane transitioning mixing layer has already received considerable attention, all issues regarding the three-dimensional structure of a spatially developing mixing layer have not yet been addressed. In terms of the computations, limits imposed by boundary conditions and the expense associated with grid size and computation time make it difficult to evaluate the structure of a spatially developing mixing layer. The appearance of mean streamwise vorticity in time-averaged measurements confirmed the existence of coherent spatially stationary secondary vorticity in mixing layers (Bell & Mehta 1992). However, details and interactions of the secondary structure are lost through the averaging process. The use of partial vorticity (Huang & Ho 1990) and Taylor's hypothesis (Nygaard & Glezer 1991; Tung 1992) in interpreting measurements obviously adds to the uncertainty. Extensive comparisons of the measured phase-averaged spanwise and streamwise vorticity were recently made to their counterparts inferred using Taylor's hypothesis (LeBoeuf & Mehta 1995*b*). The results clearly demonstrated that using Taylor's hypothesis introduces large errors, both in the shapes and levels of the vorticity contours, especially in the roller pairing region.

The main objective of this study was to investigate the development of three-dimensionality and evolution through a spanwise roller pairing in a forced plane two-stream mixing layer developing from laminar boundary layers. Acoustic forcing was used to phase-lock a specific pairing mechanism which would otherwise occur randomly in an unforced mixing layer. Phase-averaged measurements were then used to quantify the resulting vorticity development and interaction. These measurements, coupled with the previous direct numerical simulation results, shed new light on the structural development of spatially evolving (transitioning) mixing layers.

2. Experimental apparatus and techniques

The experiments were conducted in a mixing layer wind tunnel specifically designed for free-shear flow experiments (Bell & Mehta 1989). The wind tunnel consists of two separate legs which are driven independently by centrifugal blowers connected to variable speed motors. The two streams merge at the sharp trailing edge of a slowly tapering splitter plate; the included angle at the splitter plate edge, which extends 15 cm into the test section, is about 1°. The test section is 36 cm in the cross-stream (Y) direction, 91 cm in the spanwise (Z) direction, and 366 cm in length. An adjustable sidewall is used to make the streamwise pressure gradient zero. To facilitate three-dimensional traversing, a slotted aluminum plate was mounted on the traverse which moves the probe in the streamwise (X) direction. The plate, which slides against the inside surface of the sidewall, was large enough to allow traversing in the streamwise direction a distance of approximately 30 cm.

In the present experiments, the two sides of the mixing layer were set to 12 m s^{-1} and 7.2 m s^{-1} for a velocity ratio equal to that used by Bell & Mehta (1992) in the same facility, $r = U_2/U_1 = 0.6$ [$\lambda = (U_1 - U_2)/(U_1 + U_2) = 0.25$]. This gave a maximum Reynolds number, based on mixing layer thickness (δ) and velocity difference across the layer (U_0), of 3150 at the last measurement location (X = 28 cm). These operating conditions resulted in the lowest unsteadiness levels in the incoming laminar boundary layers and streamwise and transverse free-stream turbulence intensities of approximately 0.15% and 0.05%, respectively. The free stream was found to be uniform to within 0.5% and cross-flow angles were less than 0.25°. The boundary layers on the splitter plate were laminar and nominally two-dimensional at these operating conditions.

Velocity measurements were made using a single cross-wire probe which was rotated in order to obtain data in two-coordinate planes (uv and uw). The Dantec cross-wire probe (Model 55P51) consisted of 5 μm platinum-plated tungsten sensing elements approximately 1 mm long with approximately 1 mm spacing. The probes were calibrated statically in the free stream assuming a 'cosine-law' response to yaw, with the effective wire angles determined by calibration. The analog signals generated by DISA (Model 55M01) anemometers were sampled using a Tustin (Model 110-9C) 15 bit simultaneous sample-and-hold A/D converter connected to a DEC MicroVax II computer.

Conversion of the hot-wire data to effective normal velocities was achieved online through the use of look-up tables. The linear reduction to actual velocity statistics afforded by the use of the cosine-law permitted rapid run-time calculation and storage of effective velocity statistics. Additional run-time savings were obtained by using 'double-buffering', a scheme whereby a block of data is acquired via the A/D converter at the same time that a previously acquired block of data is processed (Watmuff 1995). Corrections for the effects of the mean streamwise velocity gradient across the probe face were performed before the reduction to velocity statistics. This compensation was achieved using quadratic interpolation of the effective velocity statistics (in the direction normal to the plane of the wires) to the actual probe location (centred between the wires).

Owing to the large quantity of data required by this study, many aspects of this experiment were automated. The data acquisition and control systems, with the DEC computer as the platform, are shown diagramatically in figure 1. While taking data for a single run, continuously over the course of several days, the computer was able to coordinate the traversing, A/D control, blower speed control, and relative phase of forcing signals without human intervention. To ensure measurement accuracy, a number of conditions including tunnel velocity drift, hot-wire calibration drift, forcing signal variation, and traverse malfunction were tested periodically (typically every 10 minutes) during every data acquisition run.

Further reduction of the measurements to vorticity was achieved using a central difference scheme with forward and backward differences at the grid boundaries. (For a recent review of direct vorticity measurement techniques, see Wallace & Foss 1995.) Circulation, which was evaluated using an integral over a bicubic spline fit of the vorticity for individual structures was comparable to a line integral of the velocities as expected. An error analysis based upon repeatability and calibration accuracy indicated that the time-averaged mean streamwise and cross-stream velocities were accurate to within 2% and 7% of the peak velocities, respectively, and the Reynolds stress measurements were accurate to within 10–15% of the peak values. The phase-averaged streamwise velocity and cross-stream velocities were accurate to within 5%

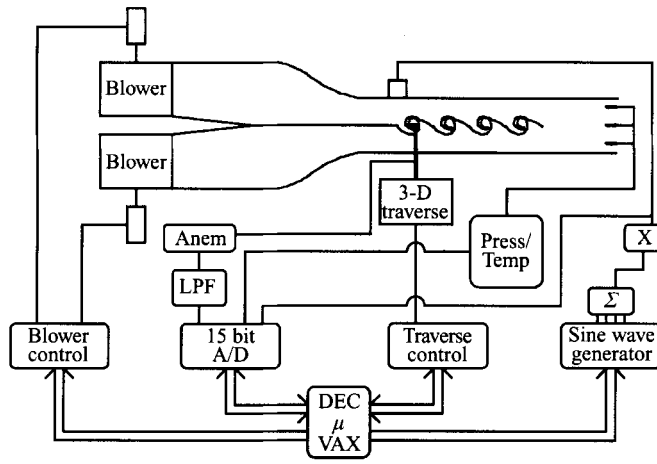

FIGURE 1. Forced mixing layer data acquisition and control system.

and 10% of the peak velocities, respectively, and the phase-averaged stresses and streamwise vorticity measurements were accurate to within 15% of the peak value.

A digital sine wave generator capable of outputting up to four signals simultaneously was built for this project. The amplitudes and frequencies were tunable from the front panel of the device while the relative phase of the sine waves could be adjusted using front panel BCD switches or digital input. Digital control of the relative phase by the computer was used during sequential runs for which the only parameter varied from one run to the next was the relative forcing signal phase. The forcing signals used to obtain the results shown in this study consisted of the sum of a sine wave and its subharmonic:

$$s(t) = A_1 \sin 2\pi f_1 t + A_2 \sin(2\pi f_2 t + \beta_2) \tag{2.1}$$

where f_1, the fundamental 'most-probable' roll-up frequency (obtained from centreline spectra in the unforced layer), was set equal to 500 Hz and f_2, the frequency corresponding to the first subharmonic, was set equal to $f_1/2 = 250$ Hz. The amplitude ratio ($a = A_2/A_1$), which largely dictates the pairing location for multiple-frequency forcing (Inoue 1992), was set equal to two for all of the measurements described in this paper. This forced the first pairing to occur between 15 and 25 cm from the splitter plate trailing edge. The individual sine waves were combined using a simple summing circuit and output by an audio amplifier to a spanwise array of three 4 inch speakers. The amplitude (volume) of the output signal from the amplifier was set to the absolute minimum level ($\sim$ 70 dB) which still gave adequate coherence in the phase-locking (§3.1). The speakers were placed directly across from the splitter plate trailing edge (see figure 1) at a sidewall slot location. The acoustic signal at the slot location was measured to be spanwise uniform to within 5%.

The sine wave generator also output digital start sample pulses and a clock signal which were used to synchronize A/D sampling with the forcing signals. For the phase-averages presented here, 768 ensembles of 16 samples per cycle were measured. The measurement grid consisted of 55 uniformly spaced X-locations in the range 1 to 28 cm and 20 uniformly spaced Y-locations distributed over a linearly increasing range of -1 to 1 cm at $X = 1$ cm to -2.5 to 2.5 cm at $X = 28$ cm. In the spanwise direction, the three-dimensional grid ranged from $Z = -5$ to 5 cm with 41 uniformly spaced locations, thus occupying the central ninth of the total test section span. The

data set therefore consisted of 16 time (or phase) steps at 45100 locations, giving a total of over 2 million phase-averaged velocity component measurements and over 3 million phase-averaged Reynolds stress measurements.

3. Results and preliminary discussion

Following convention, the velocity scale used to normalize all phase- and time-averaged data presented in the present paper is the velocity difference across the mixing layer, $U_0 = U_1 - U_2 = 4.8$ m s^{-1}

3.1. *Optimization of forcing phase: primary structure coherence*

Recognizing the importance of the structure-to-structure repeatability gained by forcing the mixing layer, the first set of measurements was used to identify the relative phase of forcing signals which gave the optimal coherence of the pairing spanwise structures. The measure of coherence used to characterize the relative success of forcing was the ratio of the periodic contribution to the Reynolds normal stress to the total Reynolds normal stress. This can be defined in terms of components identified in the traditional triple decomposition of a velocity component, $u_i(x,t)$ ($u_1 = u$, $u_2 = v$ and $u_3 = w$):

$$u_i(x,t) = \overline{u_i(x,t)} + \langle u_i(x,t)\rangle + u_i''(x,t) \tag{3.1}$$

where $\overline{u_i(x,t)}$ is the local time-average, $\langle u_i(x,t)\rangle$ is the periodic contribution, and $u_i''(x,t)$ is the random component of $u_i(x,t)$. The overbar denotes time-averaging while the brackets ($\langle\rangle$) denote a phase-locked ensemble average (phase-average) over one fundamental period. The total 'unsteadiness' is therefore defined as

$$u_i' = \langle u_i(x,t)\rangle + u_i''(x,t) \tag{3.2}$$

and the coherence parameter is given by:

$$C_i = \frac{\overline{\langle u_i(x,t)\rangle^2}}{\overline{u_i'^2}}. \tag{3.3}$$

This quantity, calculated for the u- and v-components, was averaged over a centreplane oriented normal to the mixing layer (X, Y-plane) for nine different relative phases (β_2) ranging from 0 to 180°. Note that the phase is defined such that the forcing signal repeats for every 180° shift of the subharmonic relative to the fundamental (equation (2.1)). The resulting distribution of the average coherence versus relative forcing signal phase is shown in figure 2. Clearly, the coherence displays a broad peak between approximately 0° and 45°, while the minimum is much sharper at $\beta_2 = 90°$. This relationship between the coherence and relative phase resembles the subharmonic amplification rate measured in the near-field of a double-frequency forced mixing layer by Zhang, Ho & Monkewitz (1985). In fact, Yang & Karlsonn (1991) demonstrated that low subharmonic mode growth is associated with the occurrence of shredding. Shredding is an interaction whereby every second primary vortex stops growing and is absorbed by its neighbours. When this process occurs slowly it is sometimes denoted as 'slow tearing' or 'bleeding' in contrast to 'fast tearing' in which a vortex is rapidly 'broken' by its neighbours (Hernan & Jimenez 1982). A relationship between the relative phase and vortex pairing dynamics was also observed in the present study. This is shown in figure 3(*a, b*) which contains the centerplane phase-averaged spanwise vorticity contours for the two extreme coherence cases,

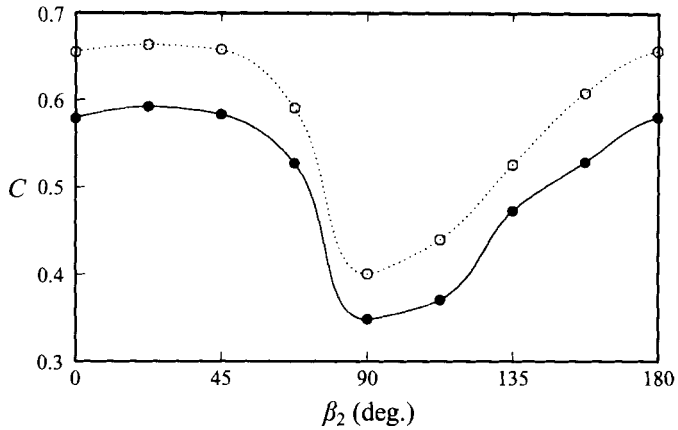

FIGURE 2. Centreplane average coherence: u (•); v (○).

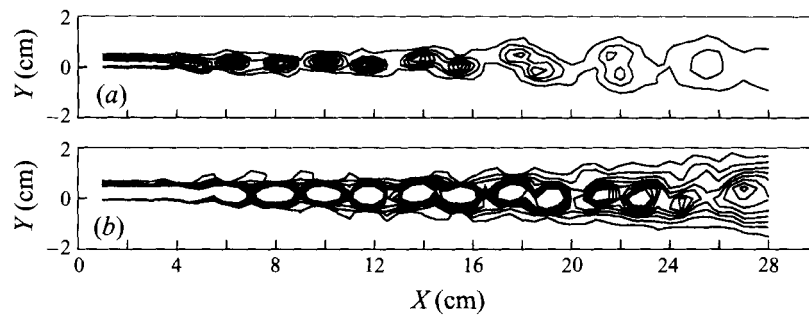

FIGURE 3. Centreplane phase-averaged spanwise vorticity ($\langle\Omega_z\rangle/U_0$, cm^{-1}) at phase 1. Lowest contour level = −0.25, increment = −0.5. (*a*) $\beta_2 = 22.5°$; (*b*) $\beta_2 = 90°$.

$\beta_2 = 22.5°$ and $\beta_2 = 90°$, respectively. Clearly, figure 3(*a*) illustrates the traditional pairing mechanism where two adjacent vortices begin to corotate and finally merge into a single larger vortex (rolling interaction). This results in a higher coherence than the shredding mechanism illustrated in figure 3(*b*). These results confirm that double-frequency forcing with a relative phase of 90° results in shredding/tearing as shown by Riley & Metcalfe (1980) using a two-dimensional temporal simulation. Furthermore, these results support the implication of the instability-wave analysis of Monkewitz (1988), that shredding occurs for only a narrow range of subharmonic to fundamental relative phases. Double-frequency forcing with relative phase (β_2) set equal to 22.5° was therefore chosen for the present measurements of the usual rolling interaction pairing mechanism.

In order to further examine this observed difference of the mean coherence parameter, the spatial distributions of the coherence parameter for the two extreme phases ($\beta_2 = 22.5°$ and $\beta_2 = 90°$) are included in figures 4 and 5, respectively. The relatively higher average u-component phase coherence for the optimum phase setting results from the recovery of the coherence near the onset of pairing ($X = 15$ cm) and the minor recovery at the edges of the mixing layer after pairing (see figures 4*a* and 5*a*). Figures 4(*b*) and 5(*b*) show that at the optimum phase, the v-component coherence recovers to its peak value immediately after pairing. This recovery does not occur for the shredding interaction.

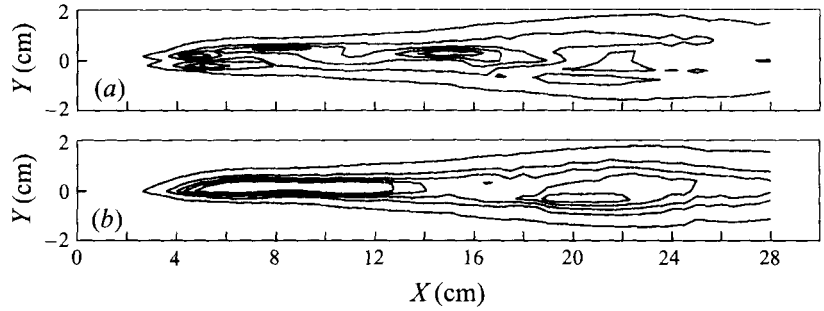

FIGURE 4. Centreplane coherence distribution for $\beta_2 = 22.5°$. (*a*) *u*, (*b*) *v*. Lowest contour level = 0.05, increment = 0.225.

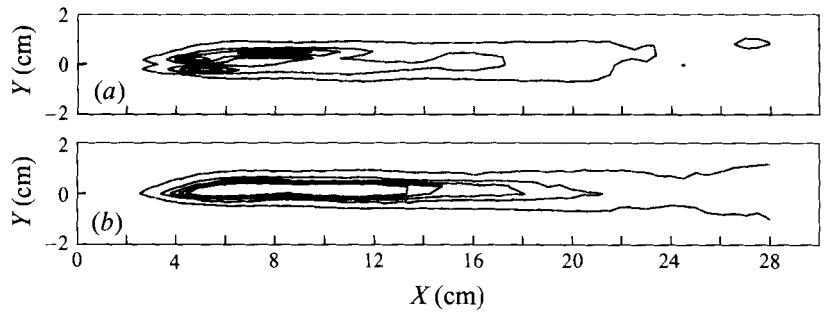

FIGURE 5. Centreplane coherence distribution for $\beta_2 = 90°$. (*a*) *u*, (*b*) *v*. Lowest contour level = 0.05, increment = 0.225.

3.2. *'Two-dimensional' spatio-temporal development*

The streamwise evolution of spanwise vorticity along the mixing layer centreline ($Z = 0$) is depicted in figure 6(*a–d*) for four phases (or times). In effect, every fourth phase out of the 16 measured phases per subharmonic cycle is presented. The evolution and pairing of sets of primary rollers can be easily tracked through the four phases shown. The initial spanwise vortex roll-up occurs at $X \approx 5$ cm. Clearly, signs of subharmonic forcing are present early in the mixing layer development since distinguishable pairs of primary rollers are discernable from the onset of their development. Spanwise vortices of each pair start to move closer together between $X \approx 10$ and 15 cm, begin to corotate at $X \approx 15$ cm, and complete the first pairing by $X \approx 25$ cm. The peak phase-averaged spanwise vorticity levels drop by a factor of about three during the pairing process. This decrease could be attributed, in part, to a loss of coherence of the primary structure. However, as figure 4 indicates, the coherence is quite good, even in the region downstream of the pairing, especially for the *v*-component.

Note that at a given phase, structure-to-structure differences in the phase-averaged quantities characterize the changes induced in a structure as it progresses downstream during one cycle of the forcing signal. Furthermore, at a given streamwise location, progression in phase illustrates the state of a structure which was upstream at an earlier phase. Of course, if no evolution takes place as a structure moves downstream, progression in phase could be used to characterize spatial development which would mean that Taylor's frozen field hypothesis would be applicable. However, it is clearly apparent that even the qualitative features of individual structures change as

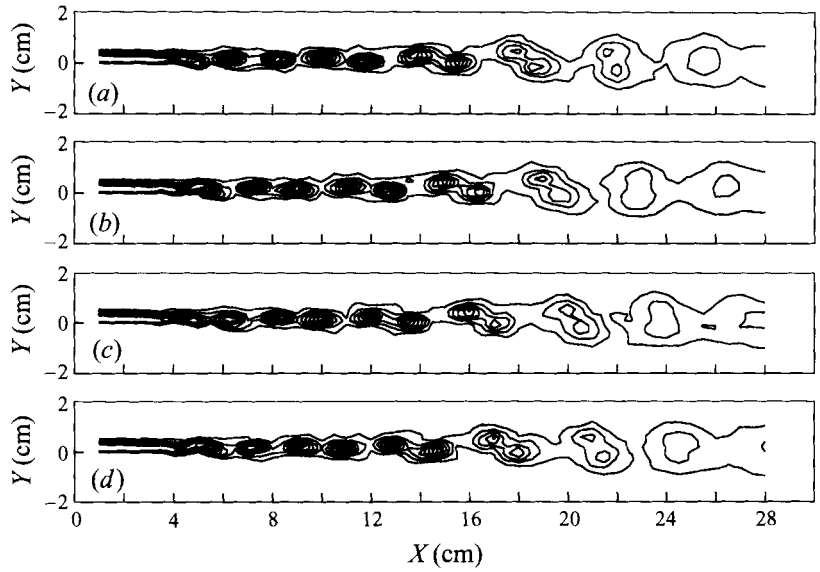

FIGURE 6. Centreplane phase-averaged spanwise vorticity ($\langle\Omega_z\rangle/U_0$, cm^{-1}) contours at various phases. Lowest level = −0.25, increment = −0.5. (*a*) Phase 1; (*b*) phase 5; (*c*) phase 9; (*d*) phase 13.

the structures evolve spatially. In fact, relatively large errors are introduced when employing Taylor's hypothesis to evaluate vorticity development in three-dimensional mixing layers as recently demonstrated by LeBoeuf & Mehta (1995*b*).

3.3. *Three-dimensional vortical structure*

3.3.1. *Initial spanwise vortex roll-up region*

A three-dimensional view of the phase-averaged spanwise vorticity ($\langle\Omega_z\rangle/U_0$) iso-surface with a chosen level of −2.0 cm^{-1} in the subdomain ranging from $X = 1$ cm to $X = 15$ cm is shown in figure 7. Included as figure 8(*a*) and 8(*b*) are the iso-surfaces of streamwise vorticity in the same subdomain with levels −0.2 cm^{-1} and 0.2 cm^{-1}, respectively. The iso-surface levels for figures 7 and 8 were chosen to provide as much detail of the three-dimensional structure as possible while maintaining figure legibility. Although the spanwise vorticity sheet coming off the splitter plate appears nominally two-dimensional (figure 7), once it rolls up into a spanwise vortex, distinct 'kinks' in the spanwise direction are apparent. These kinks appear to persist as the spanwise roller evolves further downstream. There is some evidence of the familiar streamwise vortices in the braid regions (ribs) connecting adjacent spanwise vortex rollers (figure 8). However, it is noteworthy that much of the streamwise vorticity in this subdomain appears within the spanwise rollers.

Details of the vortical structures can be examined more closely by using two-dimensional 'cuts' (with additional contour levels) through the three-dimensional data. A longitudinal (X, Y-plane) cut through the data for this subdomain along the centreline ($Z = 0$) at phase 1 is shown in figure 9 for reference. The Kelvin–Helmholtz instability seems to affect the layer at $X \approx 3.5$ cm and the first spanwise vortex begins to roll up in the region $X = 4$ to 5 cm. Presumably, the first fully rolled-up spanwise vortex is the detached one at $X \approx 6.5$ cm. The Kelvin–Helmholtz wavelength of the spanwise structures is about 2 cm. In order to get a better insight into the evolution of the streamwise vortical structures, cross-stream (Y, Z-plane) contours of

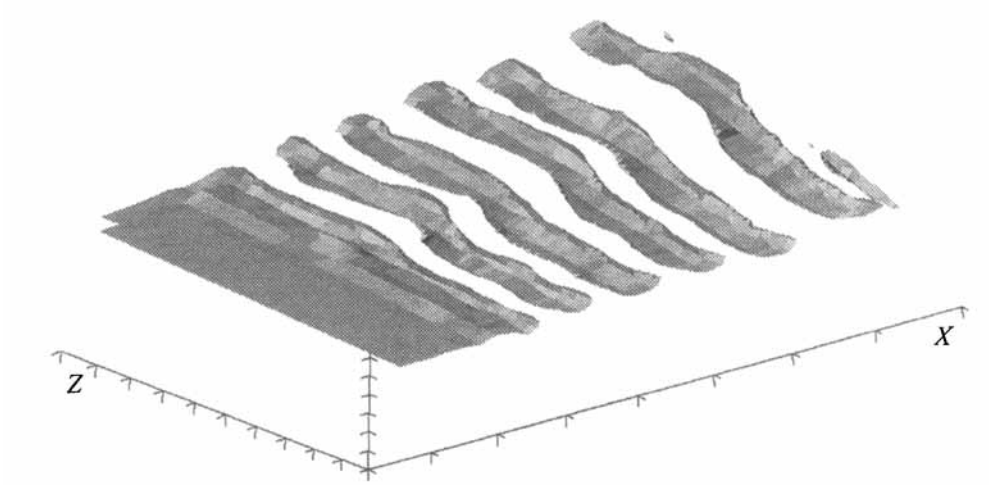

FIGURE 7. Three-dimensional view (from the low-speed side) of a spanwise vorticity iso-surface in the upstream domain ($1 < X < 15$ cm) at phase 1. $\langle\Omega_z\rangle/U_0$ (cm^{-1}) = −2.0.

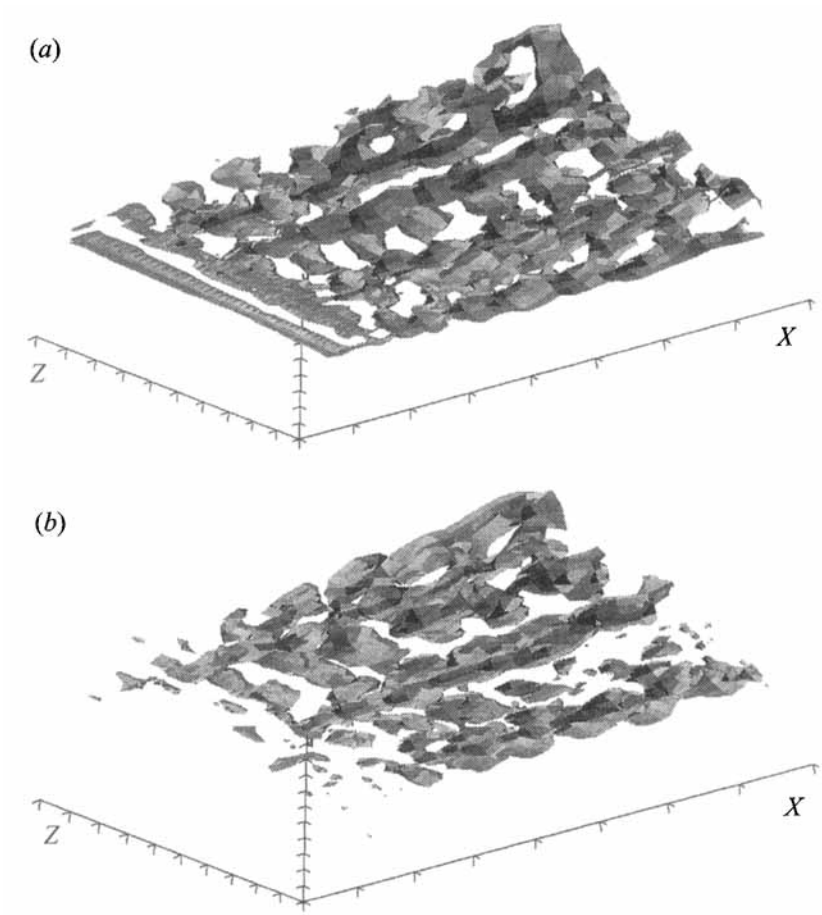

FIGURE 8. Three-dimensional view (from the low-speed side) of a streamwise vorticity iso-surface in the upstream domain ($1 < X < 15$ cm) at phase 1. (*a*) $\langle\Omega_x\rangle/U_0$ (cm^{-1}) = −0.2; (*b*) $\langle\Omega_x\rangle/U_0$ (cm^{-1}) = 0.2.

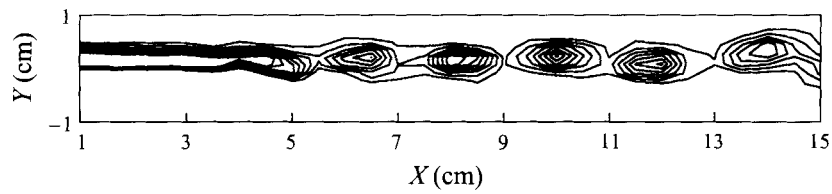

FIGURE 9. Centreplane phase-averaged spanwise vorticity ($\langle\Omega_z\rangle/U_0$, cm^{-1}) contours at phase 1 in the upstream domain. Lowest level = −0.5, increment = −0.5.

phase-averaged streamwise vorticity (at phase 1) for X ranging from 1 cm to 8.5 cm are shown in figure 10(*a–p*).

These contour plots clearly show that there is a distinct *lack* of any strong, organized streamwise vorticity in the boundary layers coming off the splitter plate (figure 10*a–d*). The first signs of any significant streamwise vorticity are seen at $X = 3$ cm (figure 10*e*). This location is just *upstream* of the first spanwise roller which, at this phase, has not yet peeled away from the initial shear layer (figure 9). A more developed state of streamwise vorticity, with higher levels and more organized distribution, is observed at $X = 4.5$ cm (figure 10*h*) which cuts right through the core of the spanwise vortex that is still rolling up. About six to seven streamwise vortical 'structures' are evident at this location with a mean spacing of about 1.3 cm, giving a spanwise wavelength of 2.6 cm. Note that the details of the streamwise structures (size, shape, strength and spacing) are not uniform across the measured span.

Using terminology introduced by Rogers & Moser (1992), (Y,Z)-planes at the locations $X = 4.5$, 6.5, and 8 cm (see figure 9) are representative of 'roller core planes' (i.e. they pass through the spanwise roller core) and (Y,Z)-planes at the locations $X = 5.5$ and 7.5 cm, are representative of 'mid-braid planes' (i.e. they pass through the braid region between consecutive spanwise rollers).

Rogers & Moser (1992) also defined the 'rib plane' as the (X,Y)-plane which centrally intersects a rib vortex and 'between-rib planes' as (X,Y)-planes located halfway between neighbouring rib planes. Locations of these planes can be identified using roller core plane streamwise vorticity contours (i.e. figure 10*i*, *l* and *o*). For example, (X,Y)-planes at $Z = 0.25$ and 2.0 cm represent rib planes while that at $Z = 1.25$ represents a between-rib plane. The spanwise and streamwise vorticity contours for these planes are included as figure 11(*a–c*) and 12(*a–c*), respectively.

The spanwise vorticity contours (figure 11) through the rib and between-rib planes appear quite similar, both in terms of qualitative (structural) features and vorticity levels. The cups of intense spanwise vorticity, observed by Buell & Mansour (1989) and Rogers & Moser (1992) in their direct numerical simulation studies were not found in the present investigation. The formation of cups was attributed to the effects of alternating stretching and compression of the primary rollers by collapsed rib vortices.

The (X,Y)-planes of streamwise vorticity through the rib and between-rib planes certainly show some obvious differences. In addition to the rib vortices, *opposite-sign* streamwise vorticity peaks appear within the spanwise roller core in the rib planes (figure 12*a* and *c*). This effect is attributable to (streamwise) kinking of the spanwise roller (figure 7) and its appearance here is consistent with the simulation results of Buell & Mansour (1989) and Rogers & Moser (1992) and with the measurements of Lasheras & Choi (1988), Nygaard & Glezer (1991) and Tung (1992). Since the deflection of the spanwise roller reaches a maximum and therefore has only a spanwise

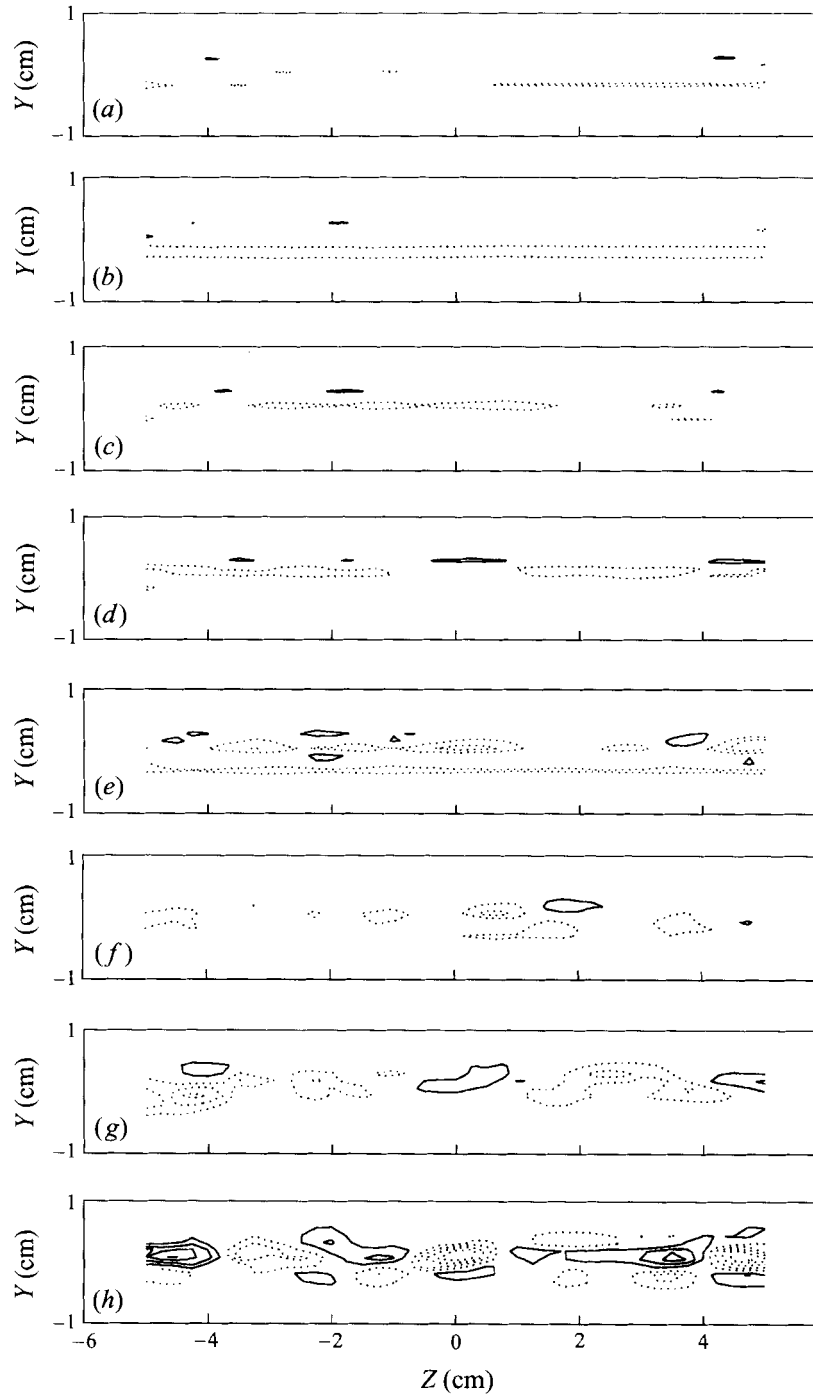

FIGURE 10 (*a–h*). For caption see facing page.

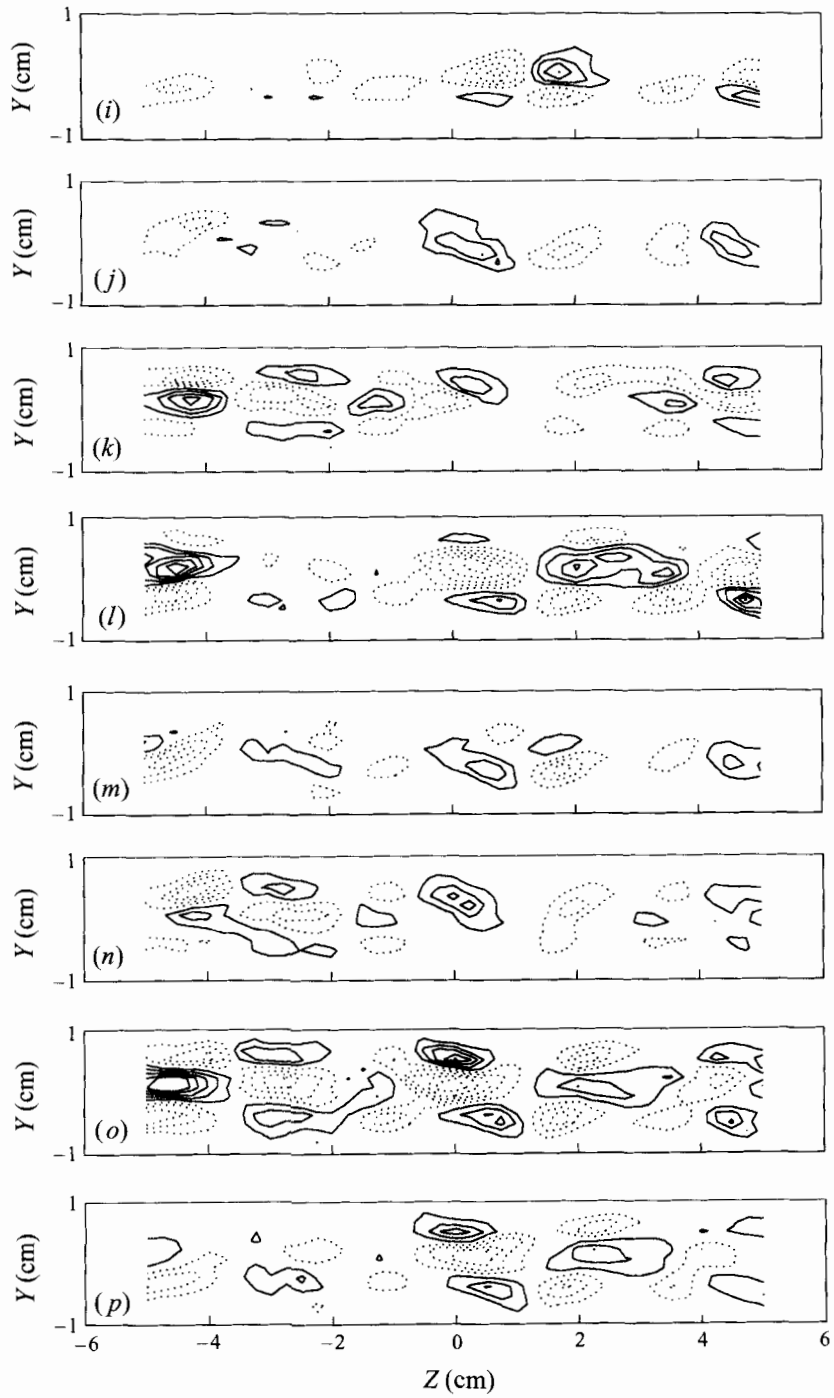

FIGURE 10. Cross-stream plane phase-averaged streamwise vorticity ($\langle\Omega_x\rangle/U_0$, cm^{-1}) contours at phase 1; lowest level = ± 0.2, increment = ± 0.2. (*a*) $X = 1$ cm; (*b*) 1.5 cm; (*c*) 2 cm; (*d*) 2.5 cm; (*e*) 3 cm; (*f*) 3.5 cm; (*g*) 4 cm; (*h*) 4.5 cm; (*i*) 5 cm; (*j*) 5.5 cm; (*k*) 6 cm; (*l*) 6.5 cm; (*m*) 7 cm; (*n*) 7.5 cm; (*o*) 8 cm; (*p*) 8.5 cm. In this and subsequent similar figures dotted lines denote negative contours and solid lines positive contours.

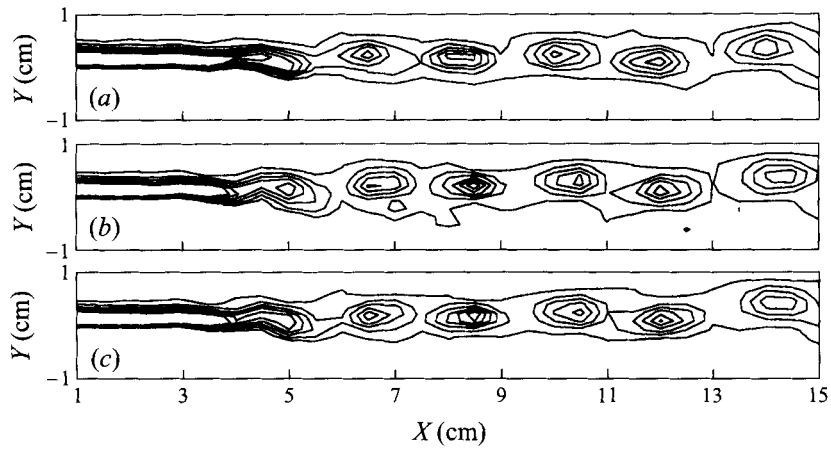

FIGURE 11. Phase-averaged spanwise vorticity ($\langle\Omega_z\rangle/U_0$, cm^{-1}) contours at phase 1. Lowest level = −0.25, increment = −0.75. (*a*) Rib plane through positive rib, Z = 0.25 cm; (*b*) between-rib plane, Z = 1.25 cm; (*c*) rib plane through negative rib, Z = 2 cm.

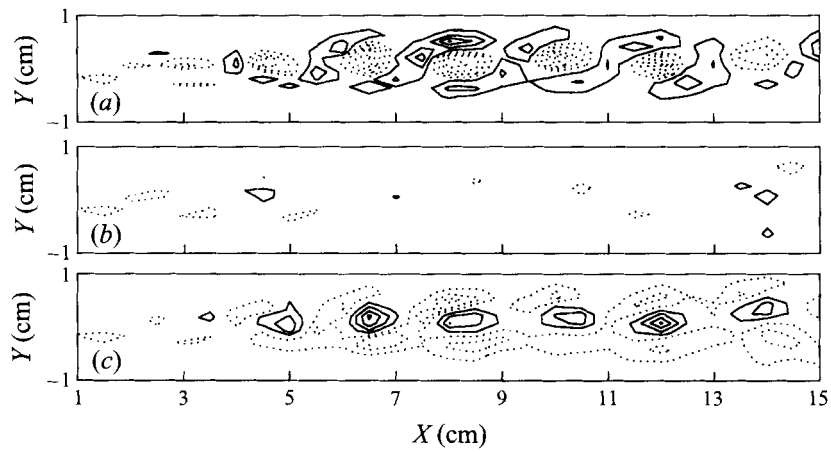

FIGURE 12. Phase-averaged streamwise vorticity ($< \Omega_x > /U_0$, cm^{-1}) contours at phase 1; lowest level = ±0.2, increment = ±0.3. (*a*) Rib plane through positive rib, Z = 0.25 cm; (*b*) between-rib plane, Z = 1.25 cm; (*c*) rib plane through negative rib, Z = 2 cm.

component in the between-rib plane (Z = 1.25 cm), its contribution is absent in that plane (figure 12*b*). Intuitively one is tempted to attribute the generation of the opposite-signed streamwise vorticity to (vertical) kinking of the roller by induced upwash/downwash effects of the counter-rotating ribs followed by tilting (in the streamwise direction) due to the velocity gradient across the layer. However, this mechanism would produce streamwise vorticity in the roller core of the same sign as the rib. Instead, the spanwise roller kinks in a direction opposite to that given by rib and shear-induced motions. This production of opposite-signed streamwise vorticity has been explained in terms of the vortex stretching terms in the streamwise vorticity equation by Buell (1991) and Rogers & Moser (1991).

The arrangement of rib vortices and streamwise vorticity within the spanwise roller yields a three-tier arrangement of streamwise vorticity in the roller core planes

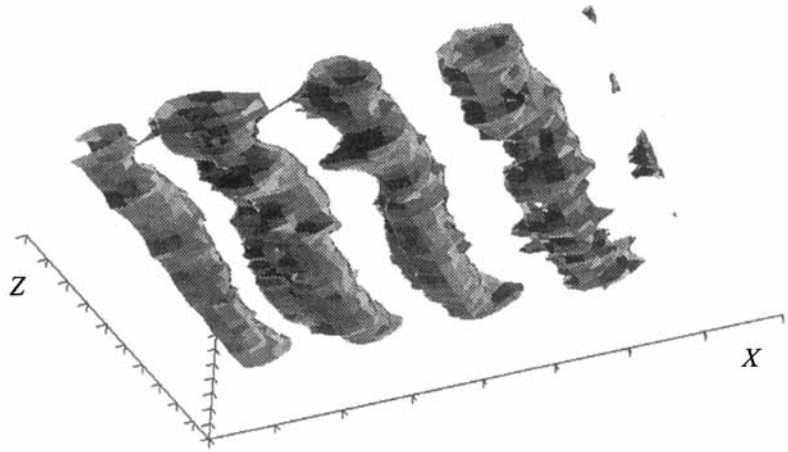

FIGURE 13. Three-dimensional view (from the low-speed side) of a spanwise vorticity iso-surface in the downstream domain ($15 < X < 28$ cm) at phase 1. $\langle\Omega_z\rangle/U_0$ (cm^{-1}) = −0.6.

(figure 10*l* and *o*) whereas in the mid-braid planes, only the rib vortices are apparent (figure 10*j* and *n*). Note that the upper rib vortices are not observed in the streamwise vorticity contours between $Z = 0$ and 2 cm in the roller core plane at $X = 5$ cm (figure 10*i*) because their amplitudes were too weak relative to the choice of contour levels. In terms of the streamwise development, the secondary structure does not appear to change much within this subdomain. The (phase-averaged) streamwise vorticity levels are generally higher in the roller core planes due to the distortion of the spanwise rollers and the fact that the rib vortices are more aligned with the mean (streamwise) flow. The maximum streamwise vorticity levels in the roller core planes due to spanwise roller distortion are comparable to those due to the ribs. The number of streamwise structures within the measured span, and hence their spacing, were maintained within this subdomain.

3.3.2. *First spanwise vortex pairing region*

A three-dimensional view of the phase-averaged spanwise vorticity ($\langle\Omega_z\rangle/U_0$) iso-surface with a level of −0.6 cm^{-1} in the subdomain ranging from $X = 15$ cm to $X = 28$ cm at phase 1 is shown in figure 13. The first pairing of the spanwise vortex rollers is clearly evident in this region. Included as figure 14(*a*) and 14(*b*) are the iso-surfaces of streamwise vorticity for the same subdomain with levels −0.2 cm^{-1} and 0.2 cm^{-1}, respectively. As in the previous subdomain, the positive and negative rib vortices are clearly evident, but less streamwise vorticity is now seen in the spanwise core regions.

Once again, details of the vortical structures are studied more closely by using two-dimensional 'cuts' through the three-dimensional data. For reference, an (X, Y)-plane cut through the data along the centreline ($Z = 0$) and at phase = 1 is presented for this subdomain in figure 15. Pairing of the spanwise rollers, which starts to occur at $X \approx 15$ cm, is completed in this region resulting in a single larger roller toward the end of this subdomain ($X \approx 25.5$ cm). As a result, the streamwise wavelength has been doubled to about 4 cm. Also, the peak spanwise vorticity levels in the amalgamated roller are significantly lower than those in the original two structures (by a factor of ~ 3).

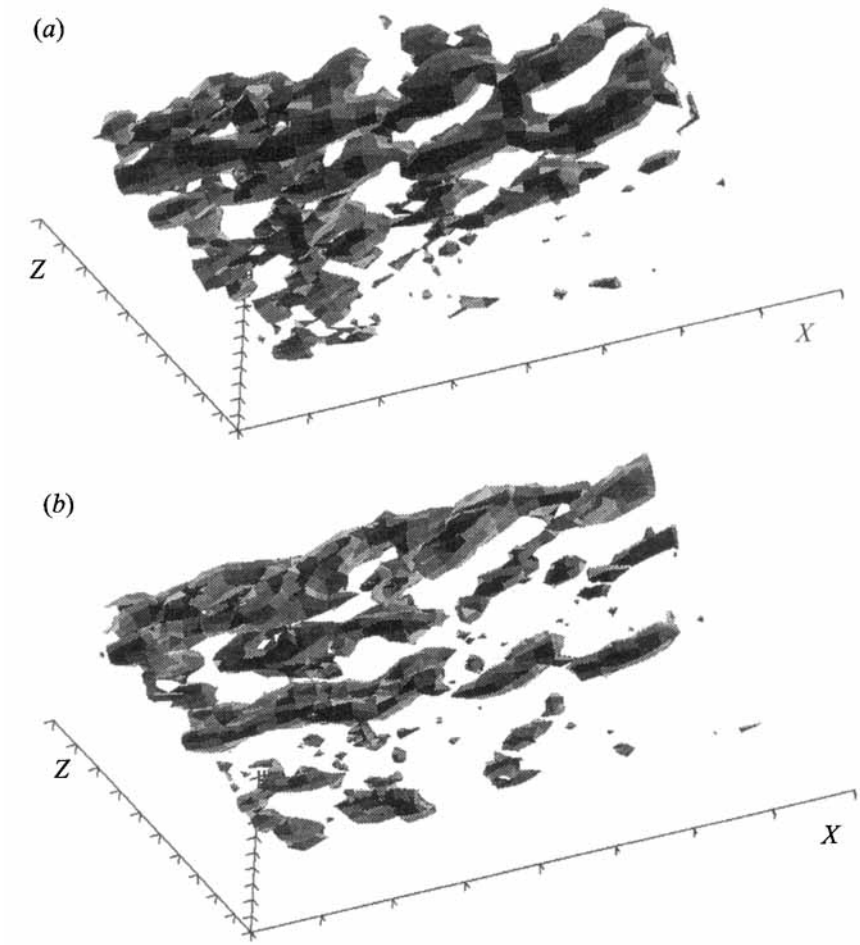

FIGURE 14. Three-dimensional view (from the low-speed side) of a streamwise vorticity iso-surface in the downstream domain ($15 < X < 28$ cm) at phase 1. (*a*) $\langle\Omega_x\rangle/U_0$ (cm^{-1}) $= -0.2$; (*b*) $\langle\Omega_x\rangle/U_0$ (cm^{-1}) $= 0.2$.

Evolution of the streamwise vorticity is first examined through cross-stream (Y, Z-plane) cuts. Figure 16(*a*)–16(*d*) correspond to roller core planes at $X = 18$, 19, 22 and 26 cm, respectively. At the onset of pairing, when two primary rollers are beginning to merge (between $X \approx 17$ and 20 cm, at this first phase), the three-tier arrangement of streamwise vorticity in the roller core planes has begun to distort, but remains identifiable (see figure 16*a* and *b*). Note that the peak phase-averaged streamwise vorticity levels have decreased by about a factor of two relative to peak amplitudes immediately after the spanwise vortex roll-up occurs. Accordingly, the maximum contour levels selected for this domain have been reduced by a factor of about two compared to those in the upstream domain discussed above in §3.3.1 (see figure 10, for example). It is evident from figure 15 that pairing is occurring between approximately $X = 17$ cm and $X = 24$ cm. A comparison of the roller core planes at $X = 22$ cm and $X = 26$ cm (figure 16*c* and *d*), indicates that reorganization (interaction) of the secondary vorticity continues to take place even towards the final stages of pairing. In particular, it appears that the roller core plane streamwise vorticity arrangement is tending toward the three-tier arrangement within a cycle

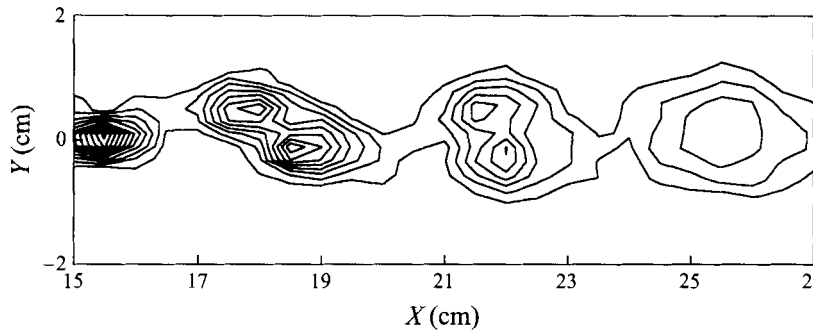

FIGURE 15. Centreplane phase-averaged spanwise vorticity ($\langle\Omega_z\rangle/U_0$, cm^{-1}) contours at phase 1 in the downstream domain. Lowest level = −0.25, increment = −0.25.

after pairing occurs (figure 16*d*). Another point to note is that a bias is developing in this subdomain such that the stronger, more organized streamwise vortices reside mostly on the positive-Z side.

Figure 17(*a*)–17(*d*) correspond to mid-braid planes at X = 16.5, 18.5, 20.5, and 23.5 cm, respectively. Within three cycles, the surviving braid region moves from X = 16.5 to 20.5 to 23.5 cm. As in the roller core planes, the stronger streamwise structures in these mid-braid plane cuts are also found on the positive-Z side. Downstream of $X \approx 20$ cm, the peak streamwise vorticity levels in the mid-braid planes are higher than those in the roller core planes (compare figure 16*c,d* and 17*c,d*). Note that the streamwise vortex spacing prior to pairing remained constant – compare the streamwise vorticity distributions at X = 5.5 cm (figure 10*j*) with those at X = 16.5 cm (figure 17*a*). The compression caused by primary rollers coming closer together at the onset of pairing causes adjoining ribs to expand or elongate and become tilted as seen in figure 17(*b*), as compared to the other mid-braid planes. Most importantly, the spanwise scale or spacing of the rib vortices has *not* increased through this first pairing, as evidenced by comparing figure 17(*a*) and 17(*d*). Thus, compared to the near-field value, the spanwise to streamwise wavelength ratio was decreased from about 1.3 to 0.65.

In the pairing and post-pairing stages of the mixing layer, rib planes and between-rib planes can be identified using the mid-braid plane streamwise vorticity contours as a guide (figure 17). For example, (X, Y)-planes at Z = 0.25 and 1.75 cm represent rib planes while that at Z = 1 cm represents a between-rib plane. The spanwise and streamwise vorticity contours for these planes are included as figure 18(*a–c*) and 19(*a–c*), respectively. As in the upstream domain, cuts showing spanwise vorticity contours through the rib planes and between-rib planes (figure 18) appear very similar and, even in this region, there are no signs of the cups of relatively strong spanwise vorticity reported for the simulation results (Buell & Mansour 1989; Rogers & Moser 1992).

As expected, the streamwise vorticity is significantly weaker in the between-rib plane (figure 19*b*), than in the adjacent rib planes (figure 19*a* and *c*). Cuts through the rib planes clearly show the form of the streamwise vorticity during the pairing process. In order to illustrate the ('spatio-temporal') evolution of the streamwise vorticity during pairing, eight phases for the rib plane cut shown in figure 19(*c*) are presented in figure 20(*a–h*). The two rollers undergoing pairing clearly exhibit the three-tier distribution as they start to rotate about each other. As they pair, the

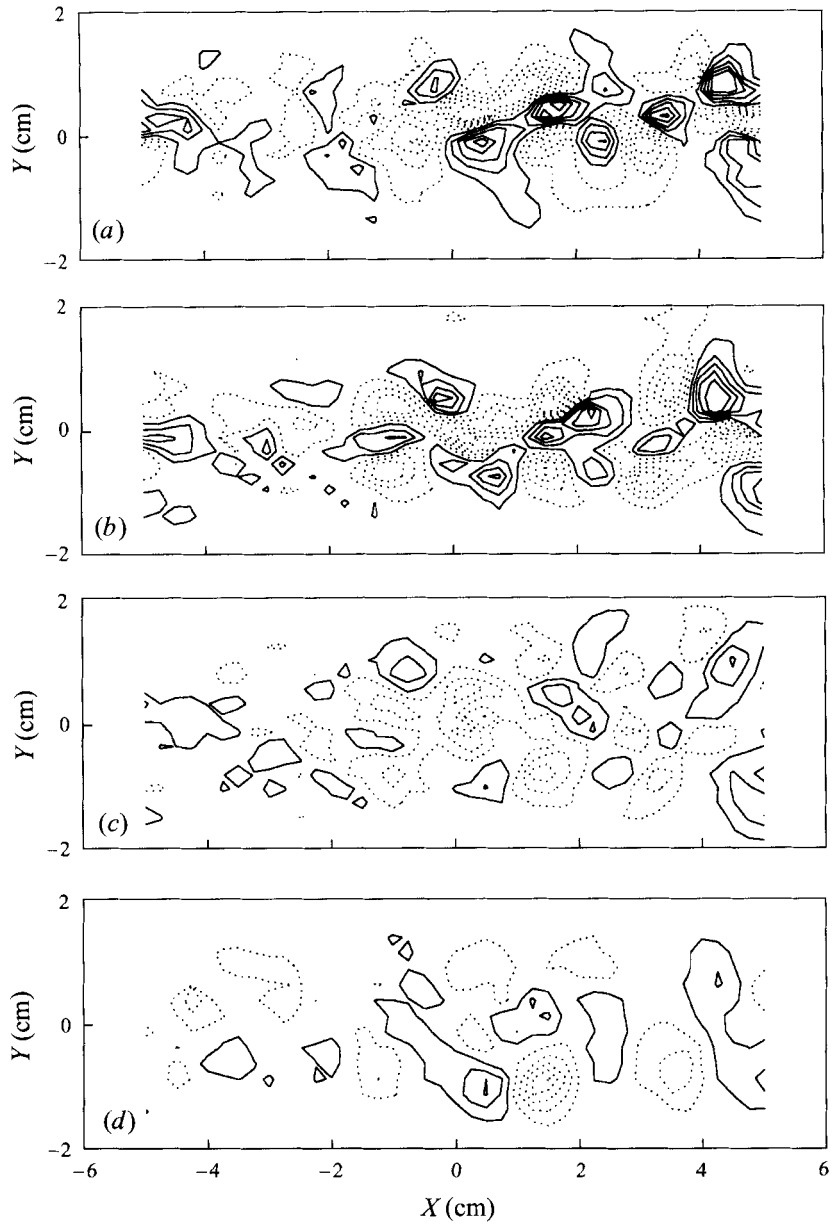

FIGURE 16. Cross-stream plane phase-averaged streamwise vorticity ($\langle\Omega_x\rangle/U_0$, cm^{-1}) contours at phase 1 through roller core planes; lowest level = $\pm$0.075, increment = $\pm$0.15. (*a*) X = 18 cm; (*b*) X = 19 cm; (*c*) X = 22 cm; (*d*) X = 26 cm.

two regions of spanwise roller core vorticity eventually coalesce, thus forming the contribution from the new core. Note that the two regions of positive streamwise vorticity at $X \approx 21.5$ cm at phase 15 (figure 20*h*) coalesce into the single region at $X \approx 22$ cm at phase 1 of the next cycle (figure 20*a*). The rib vorticity in between the two pairing rollers seems to 'disappear'. Simulation results suggest that this vorticity may be destroyed by intense vortex stretching in this region (Moser & Rogers 1993).

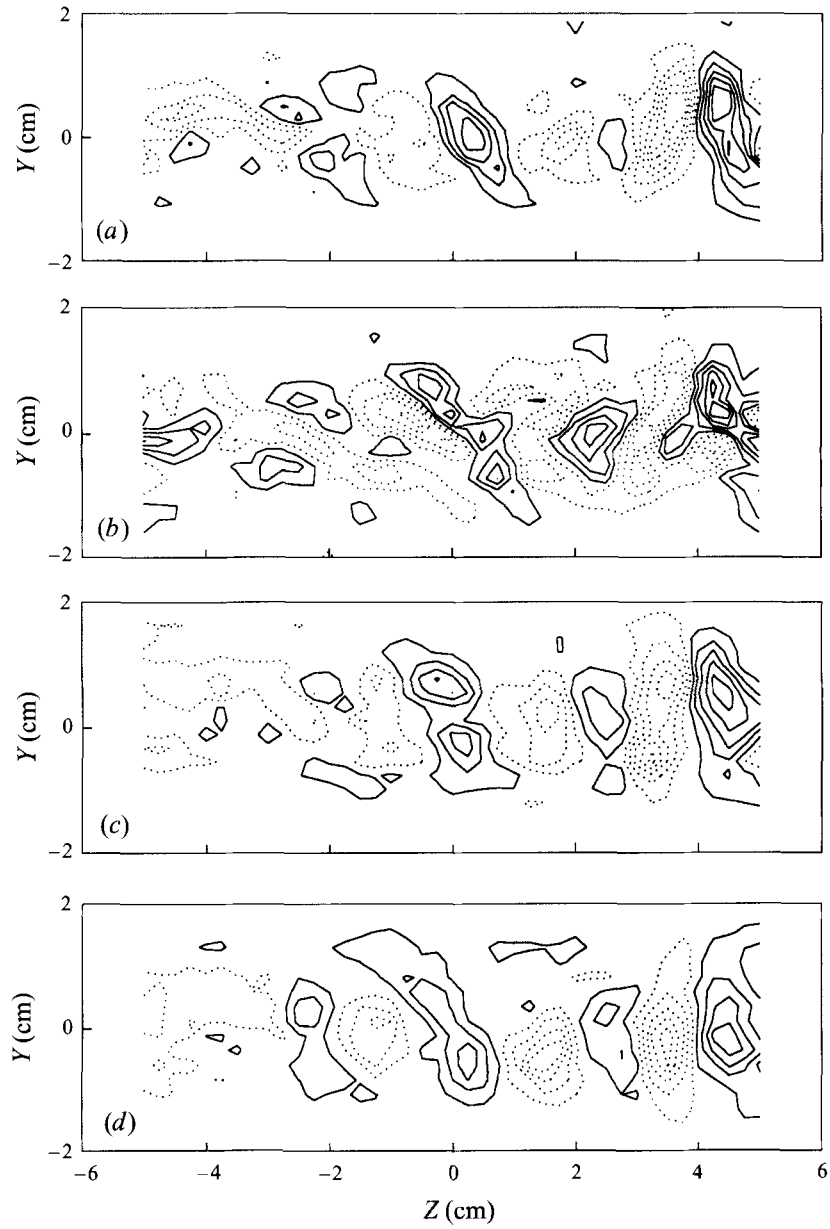

FIGURE 17. Cross-stream plane phase-averaged streamwise vorticity ($\langle\Omega_x\rangle/U_0$, cm^{-1}) contours at phase 1 through mid-braid planes; lowest level = ± 0.075, increment = ± 0.15. (*a*) $X = 16.5$ cm; (*b*) $X = 18.5$ cm; (*c*) $X = 20.5$ cm; (*d*) $X = 23.5$ cm.

Note that once the pairing process is complete ($X \approx 25$ cm), the streamwise vorticity of the rib vortices is substantially higher than that due to kinking of the primary rollers. In addition, the rib contribution to the streamwise vorticity is higher in the braid than it is in the roller core plane. This is in sharp contrast to the rib plane streamwise vorticity distribution of the initial roll-up region (figure 12*a* and *c*), where the streamwise vorticity levels in the roller core plane due to kinking are comparable to those of the rib contribution, which in turn is higher in the roller

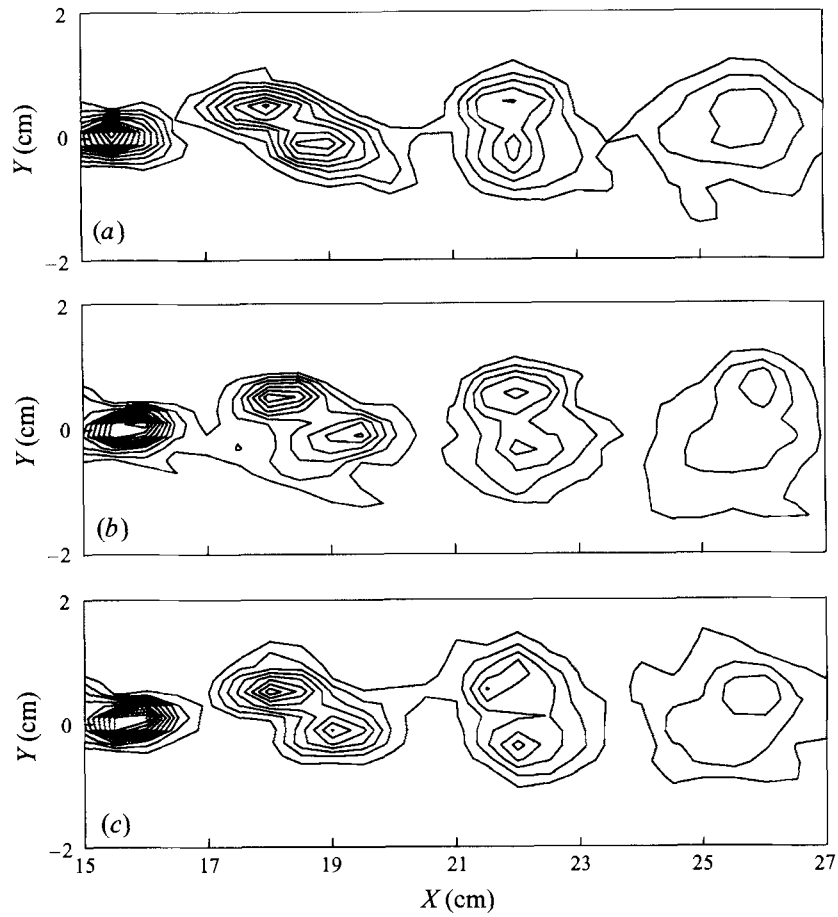

FIGURE 18. Phase-averaged spanwise vorticity ($\langle\Omega_z\rangle/U_0$, cm^{-1}) contours at phase 1. Lowest level = −0.25, increment = −0.25. (*a*) Rib plane through positive rib, Z = 0.25 cm; (*b*) between-rib plane, Z = 1 cm; (*c*) rib plane through negative rib, Z = 1.75 cm.

core plane than in the mid-braid plane. The same trends were apparent in the results of Tung (1992). The reduction of the roller contribution, which was also observed in temporal simulations by Moser & Rogers (1993), implies that either the kinking of the spanwise rollers is reduced in this downstream region or that the spanwise vorticity has decayed faster than the rib vorticity, or a combination of the two. Examination of the spanwise vorticity in the two regions (figures 7 and 13) indicates that although the rollers are still kinked during pairing, the paired structure in figure 13 is certainly more two-dimensional than the pre-paired rollers in figure 7. So this decreased kinking of the rollers is at least partly responsible for the observed effects. On examining (X, Y)-plane cuts in the region of the rib planes, it was found that the ribs are still wrapped around the rollers, but the ends are skewed in the spanwise direction, thus making their contribution to the roller core plane streamwise vorticity smaller. Further implications of this change in strength are discussed below in §4.2 and the relative strengths of the phase-averaged streamwise and spanwise vorticity are compared in §4.4.1.

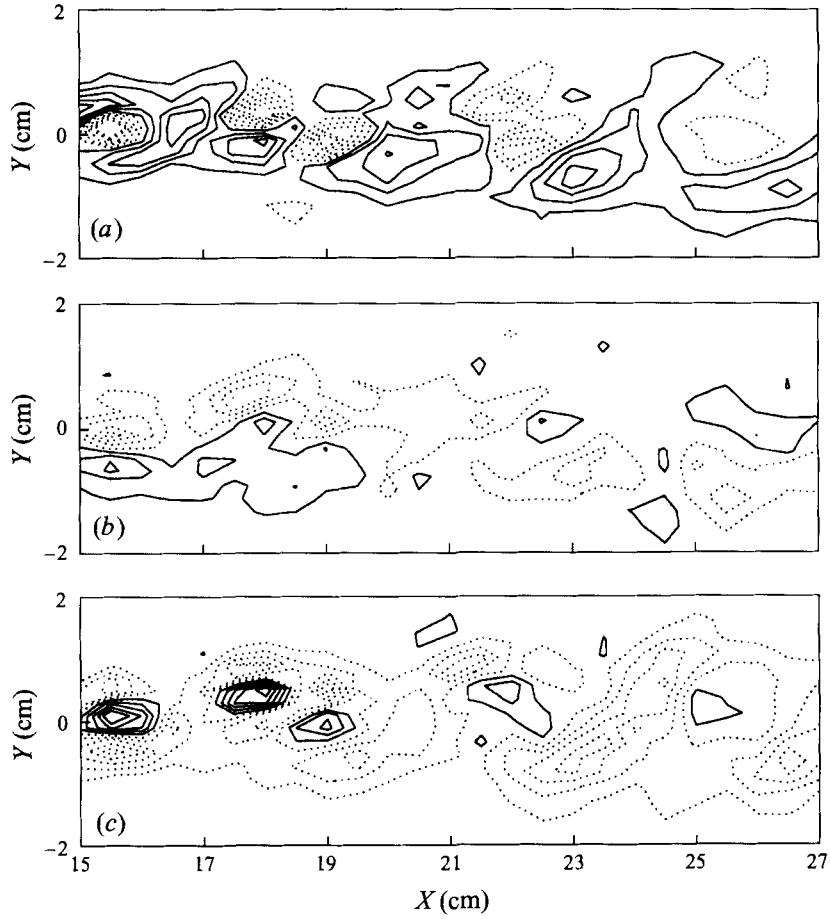

FIGURE 19. Phase-averaged streamwise vorticity ($\langle\Omega_x\rangle/U_0$, cm^{-1}) contours at phase 1; lowest level = $\pm$0.075, increment = $\pm$0.15. (*a*) rib plane through positive rib, Z = 0.25 cm; (*b*) between-rib plane, Z = 1 cm; (*c*) rib plane through negative rib, Z = 1.75 cm.

3.4. *Phase-averaged streamwise velocity and Reynolds stresses*

The effects of the three-dimensional vortical structure on the mixing layer mean and turbulence properties are examined in this subsection in terms of the phase-averaged streamwise velocity ($\langle U/U_0\rangle$) and the phase-averaged total Reynolds stress contributions ($\langle u_i'u_j'\rangle/U_0^2$), each at phase 1. The total stress, defined in terms of the total unsteadiness (equation (3.2)), includes contributions from the periodic as well as the random components.

Figure 21(*a–f*) shows longitudinal (X, Y-plane) cuts through a rib plane (Z = 0.25 cm) in the near-field region prior to pairing. The $\langle U\rangle$ contours (figure 21*a*) exhibit a curious 'pinched' effect with the locations of the pinches coinciding with those of the spanwise rollers, thus making the mixing layer thinner at the roller locations. This is caused by induced velocity effects of the spanwise rollers whereby it adds to the mixing layer streamwise velocity at the high-speed edge and reduces it at the low-speed edge. Since $\langle\Omega_z\rangle = (\partial\langle V\rangle/\partial X) - (\partial\langle U\rangle/\partial Y)$, it is perhaps not too surprising that $(\partial\langle U\rangle/\partial Y)$ is highest in the region of the spanwise roller. However, $\langle\Omega_z\rangle$ based on $\partial\langle U\rangle/\partial Y$ alone (as is often examined) looks quite different to that

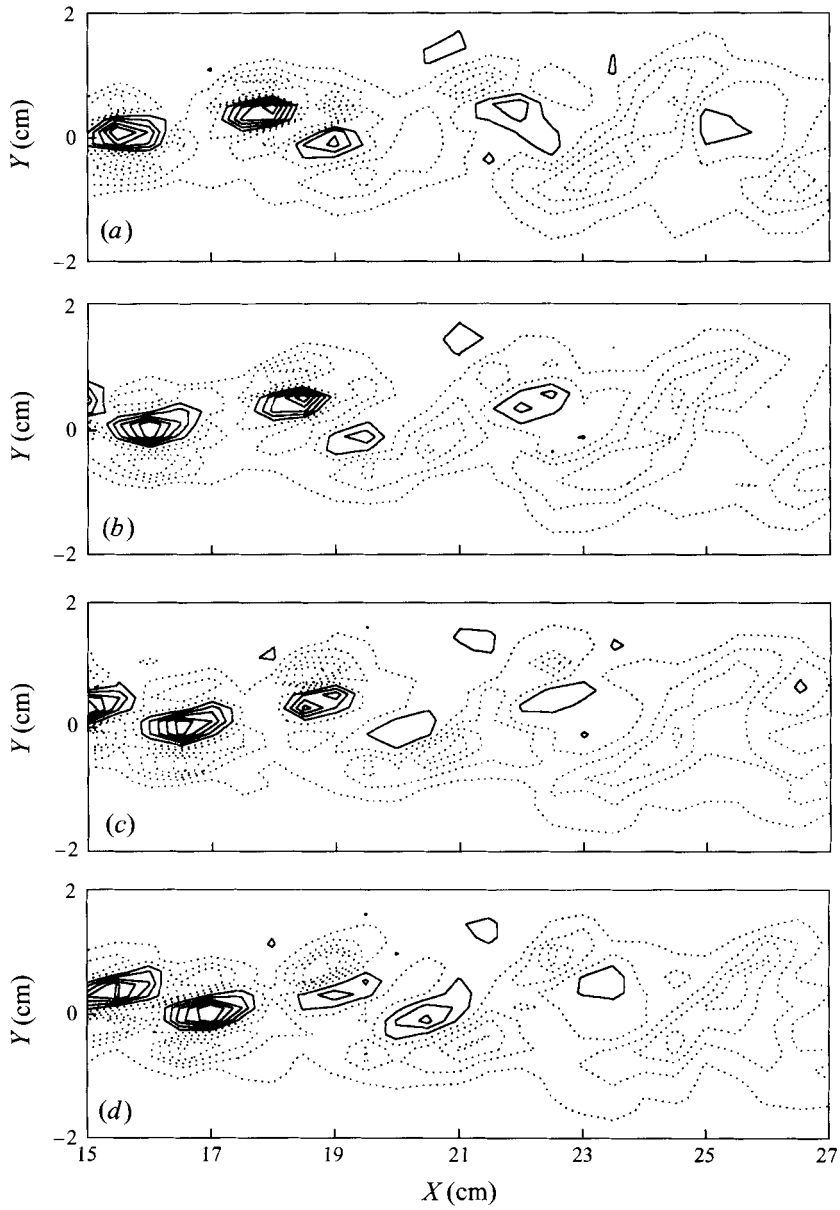

FIGURE 20 (*a–d*). For caption see facing page.

shown in figure 9, which contains the contribution of $\partial\langle V\rangle/\partial X$ as well. This is because $\partial\langle V\rangle/\partial X$ counteracts the contribution of $\partial\langle U\rangle/\partial Y$ between pairing rollers and reinforces it within the rollers.

All three normal stresses exhibit dominant peaks in the region of the spanwise vortex cores in the rib plane (figure 21*b,c,d*), although they are stronger and more apparent in the distributions of $\langle u'^2\rangle$ and $\langle v'^2\rangle$. Peaks in $\langle v'^2\rangle$ are obviously due to the strong v-fluctuation produced by the passage of spanwise rollers. Note that peaks in the $\langle u'^2\rangle$ distribution appear on each side of the mixing layer centreline ($Y = 0$) because of the positive and negative streamwise velocity perturbations induced by

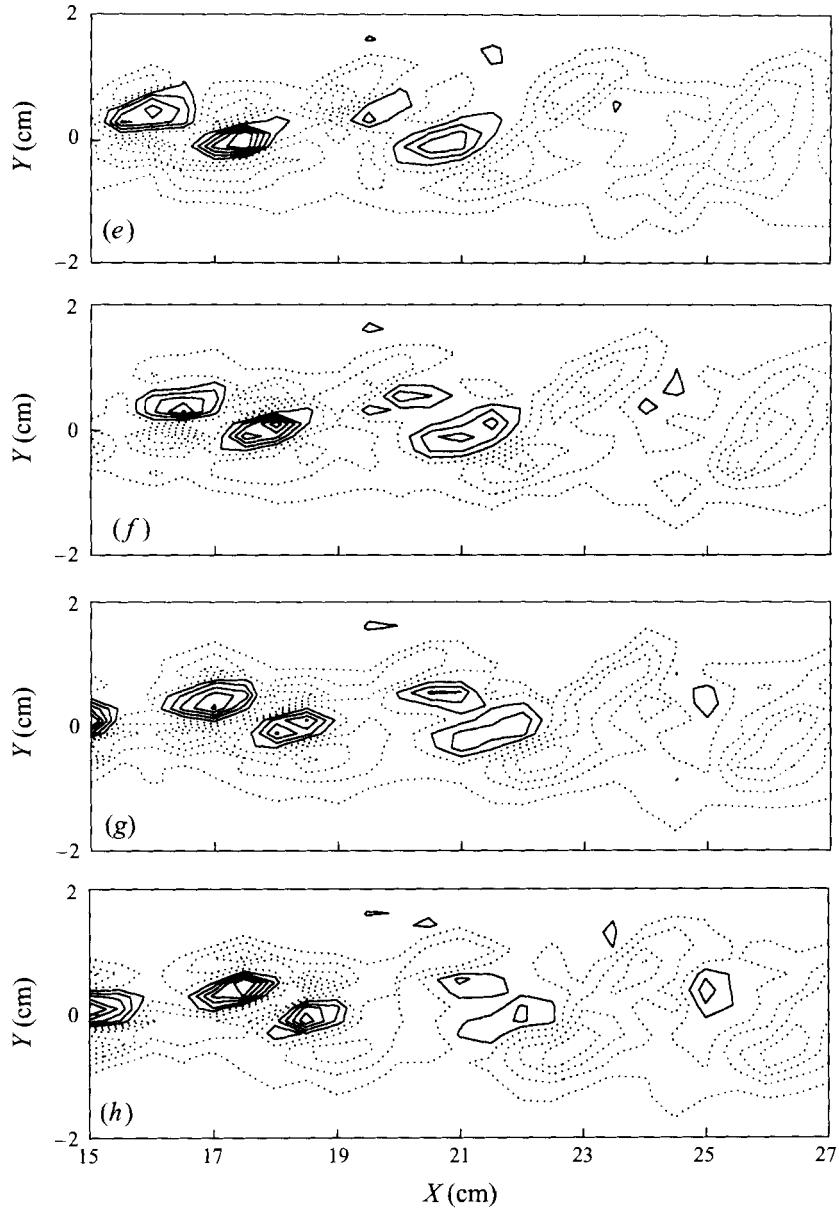

FIGURE 20. Phase-averaged streamwise vorticity ($\langle\Omega_x\rangle/U_0$, cm^{-1}) contours for a rib plane cut at $Z = 1.75$ cm in the pairing region for various phases; lowest level = ± 0.075, increment = ± 0.15. (*a*) phase 1; (*b*) phase 3; (*c*) phase 5; (*d*) phase 7; (*e*) phase 9; (*f*) phase 11; (*g*) phase 13; (*h*) phase 15.

the individual primary rollers. These local peaks of $\langle u'^2\rangle$ result in the double-peaked profile of $\overline{u'^2}$ in near-field time-averaged measurements (Bell & Mehta 1990, 1992).

The primary shear stress ($\langle u'v'\rangle$) contours (figure 21*e*) exhibit a more complex distribution. The combined effects of the roller-induced streamwise and transverse velocity fluctuations result in the quadrupole arrangement of positive and negative peaks which appears at several primary roller locations (e.g. $X \approx 9.5$–10 cm). This arrangement becomes dominated by two strong positive peaks or two strong negative

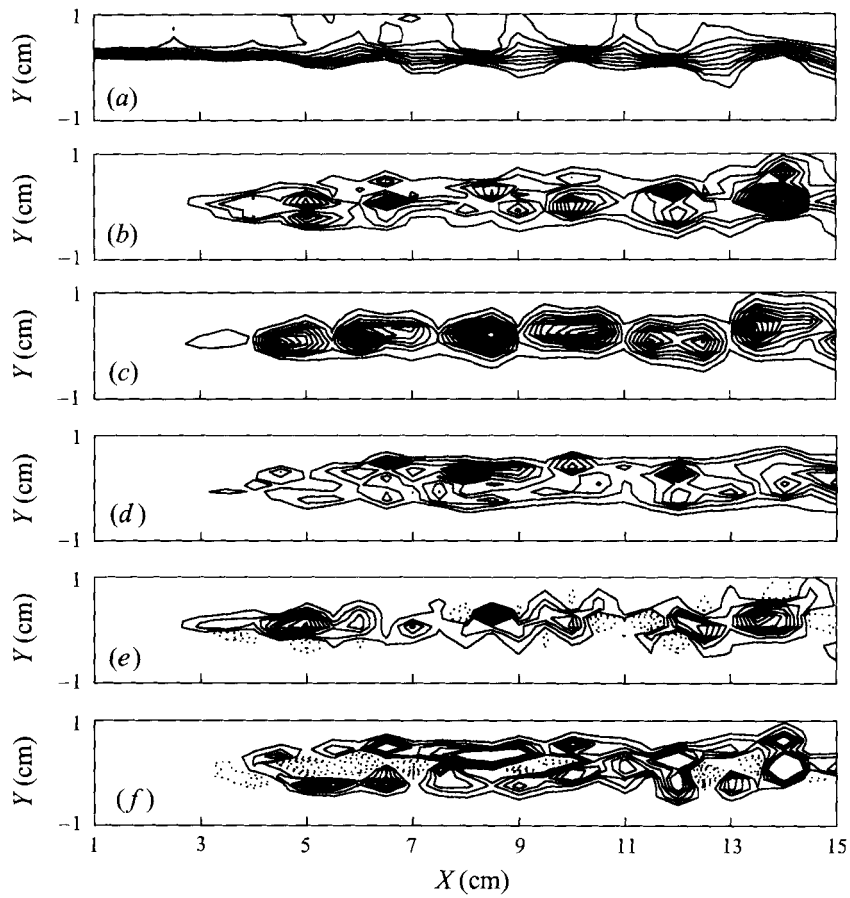

FIGURE 21. Phase-averaged streamwise velocity and Reynolds stress contours at phase 1 in the upstream domain through a rib plane (Z = 0.25 cm). (*a*) $\langle U\rangle/U_0$, lowest level = 1.6, increment = 0.1; (*b*) $\langle u'^2\rangle/U_0^2$, lowest level = 0.01, increment = 0.01; (*c*) $\langle v'^2\rangle/U_0^2$, lowest level = 0.015, increment = 0.015; (*d*) $\langle w'^2\rangle/U_0^2$, lowest level = 0.005, increment = 0.005; (*e*) $\langle u'v'\rangle/U_0^2$, lowest level = $\pm$0.005, increment = $\pm$0.01; (*f*) $\langle u'w'\rangle/U_0^2$, lowest level = $\pm$0.003, increment = $\pm$0.003.

peaks (one above and one below the core centre) for forward leaning or backward leaning elliptically shaped vortices (Ho & Huerre 1984). The positive peaks contribute to the opposite-signed primary shear stress which is often observed in time-averaged measurements in regions of zero or very low mixing layer growth (Huang & Ho 1990; Bell & Mehta 1992).

Upon careful inspection of the secondary shear stress $\langle u'w'\rangle$ (figure 21*f*), saddle points were identified at most of the primary roller core locations. Recall that beneath a positive rib (at Z = 0.25 cm), the spanwise roller is kinked forward and down (in the positive-X and negative-Y direction). This causes the primary roller to induce positive perturbations in u and negative perturbations in w at the top (positive-Y) of the roller. The signs are switched for the underside of the roller (negative-Y), and the result is a negative contribution to $\langle u'w'\rangle$, both above and below the primary roller for a positive rib as shown in figure 21(*f*). Coupled with the same u-fluctuations above and below the primary roller are the w-fluctuations due to the ribs. Above a spanwise roller, a positive rib induces a negative w-fluctuation between itself and

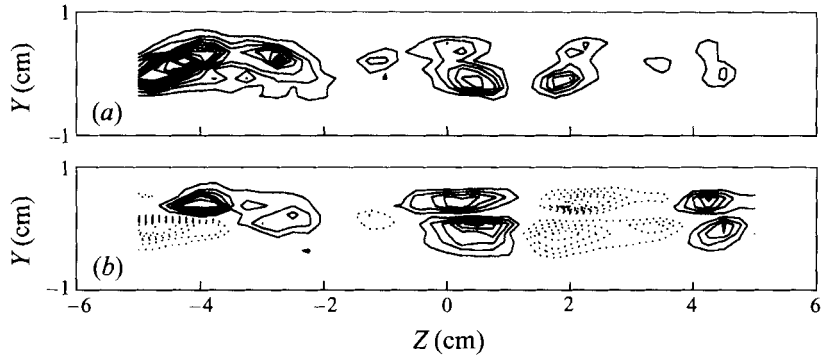

FIGURE 22. Cross-stream plane phase-averaged Reynolds stress contours at phase 1 through a mid-braid plane (X = 7.5 cm). (*a*) $\langle w'^2\rangle/U_0^2$, lowest level = 0.005, increment = 0.005; (*b*) $\langle u'w'\rangle/U_0^2$, lowest level = $\pm$0.003, increment = $\pm$0.003.

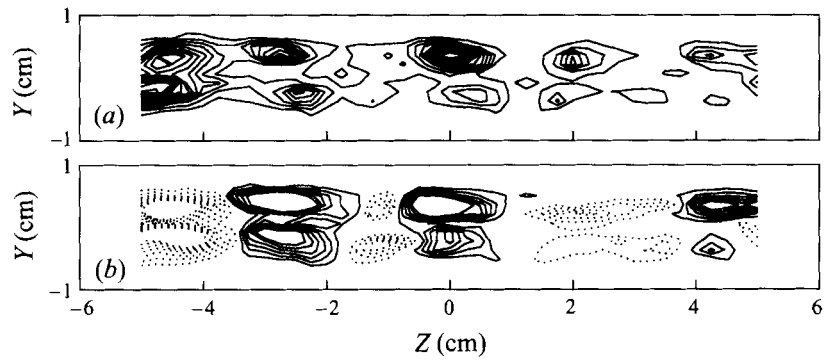

FIGURE 23. Cross-stream plane phase-averaged Reynolds stress contours at phase 1 through a roller core plane (X = 8 cm). (*a*) $\langle w'^2\rangle/U_0^2$, lowest level = 0.005, increment = 0.005; (*b*) $\langle u'w'\rangle/U_0^2$, lowest level = $\pm$0.003, increment = $\pm$0.003.

the spanwise roller and a positive w-fluctuation above itself. These fluctuations result in a reinforcement of the spanwise roller $\langle u'w'\rangle$ contribution between the rib and the primary roller while reducing the effect of the roller on $\langle u'w'\rangle$ above the rib. Apparently, the effect of the spanwise roller dominates and only negative $\langle u'w'\rangle$ peaks appear above and below the spanwise core locations.

There are also competing effects in the braid region which result in positive (or at least, much less negative) $\langle u'w'\rangle$ in that region (figure 21*f*). First note that in the braid region, fluctuations in u are negative above the centreline and positive below the centreline (see figure 21*a*). Furthermore, a positive rib would induce negative w-fluctuations below the rib (negative-Y) and positive fluctuations above it. Thus, positive streamwise vorticity in the braid region results in a negative contribution to $\langle u'w'\rangle$, both above and below the centreline. Offsetting these contributions is the effect of the kinked spanwise roller which beneath a positive rib induces a negative w-fluctuation above the centreline and positive w-fluctuations below the centreline. Coupled with the u-fluctuations, these result in a positive contribution to $\langle u'w'\rangle$, both above and below the centreline. If this contribution is strong enough, then $\langle u'w'\rangle$ will have saddle points at the spanwise roller locations (see figure 21*f*, $X \approx$ 6–7 cm). If, however, the effect of the spanwise roller kinking is not enough to offset the rib

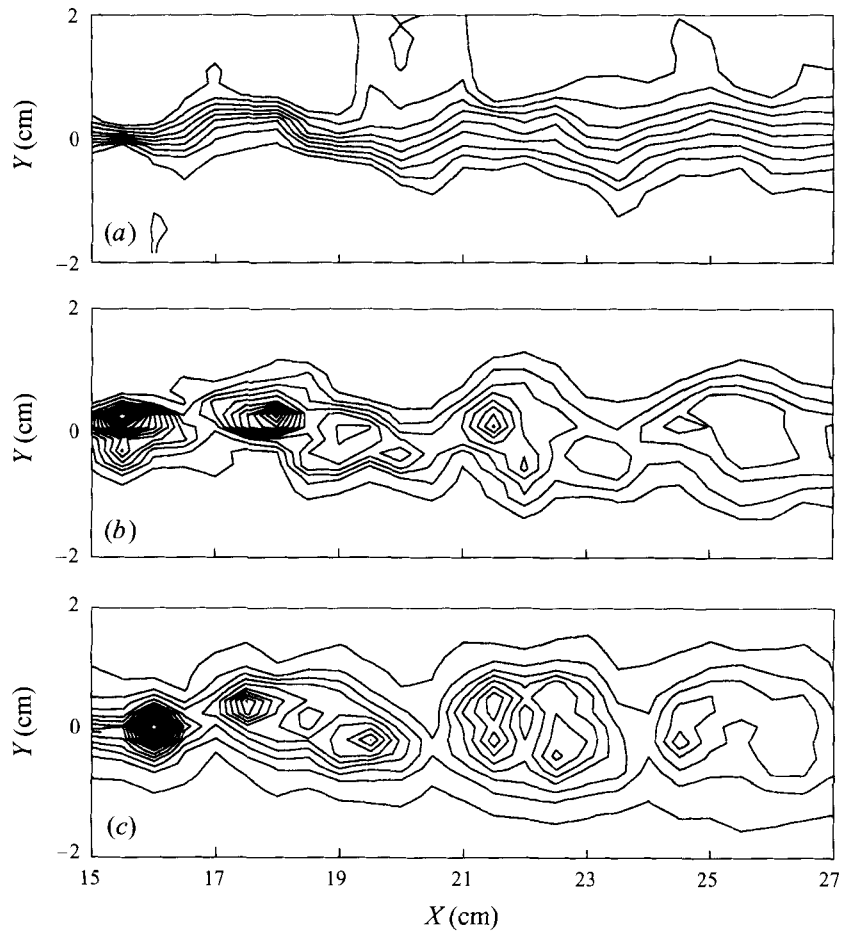

FIGURE 24 (*a–c*). For caption see facing page.

contribution, then a weak negative peak results in the braid region (see figure 21*f*, $X \approx 11$ cm). Note that for a negative rib plane all of these $\langle u'w' \rangle$ contributions will have opposite signs.

The between-rib plane contours have not been shown since the results for $\langle U \rangle$, $\langle u'^2 \rangle$, $\langle v'^2 \rangle$ and $\langle u'v' \rangle$ were qualitatively similar to those in the rib plane and contributions to $\langle w'^2 \rangle$ and $\langle u'w' \rangle$ were negligible. Demonstration of the spanwise variation of contributions to the normal, spanwise and secondary shear stress can be obtained through an examination of $\langle w'^2 \rangle$ and $\langle u'w' \rangle$ on a (cross-stream plane) mid-braid plane ($X = 7.5$ cm, figure 22) and roller core plane ($X = 8$ cm, figure 23). Clearly, in the mid-braid plane, a negative $\langle u'w' \rangle$ contribution is found above and below a positive rib ($Z \approx 0.25$ cm) and the opposite holds true for a negative rib ($Z \approx 2.0$ cm, see Ω_x, figure 10*n* and $\langle u'w' \rangle$, figure 22*b*). A comparison of roller core plane $\langle u'w' \rangle$ contours (figure 23*b*) to those of Ω_x (figure 10*o*) demonstrates the dominance of the $\langle u'w' \rangle$ contribution between the ribs and the spanwise roller core, thus yielding off-centreline peaks of the same sign as the rib streamwise vorticity. These effects of reinforcement of rib-induced spanwise vorticity above and below the primary roller also produce peaks in the roller core plane $\langle w'^2 \rangle$ contours (figure 23*a*). The lack of such reinforcement in the braid region results in a less pronounced double-peak pattern in the mid-braid

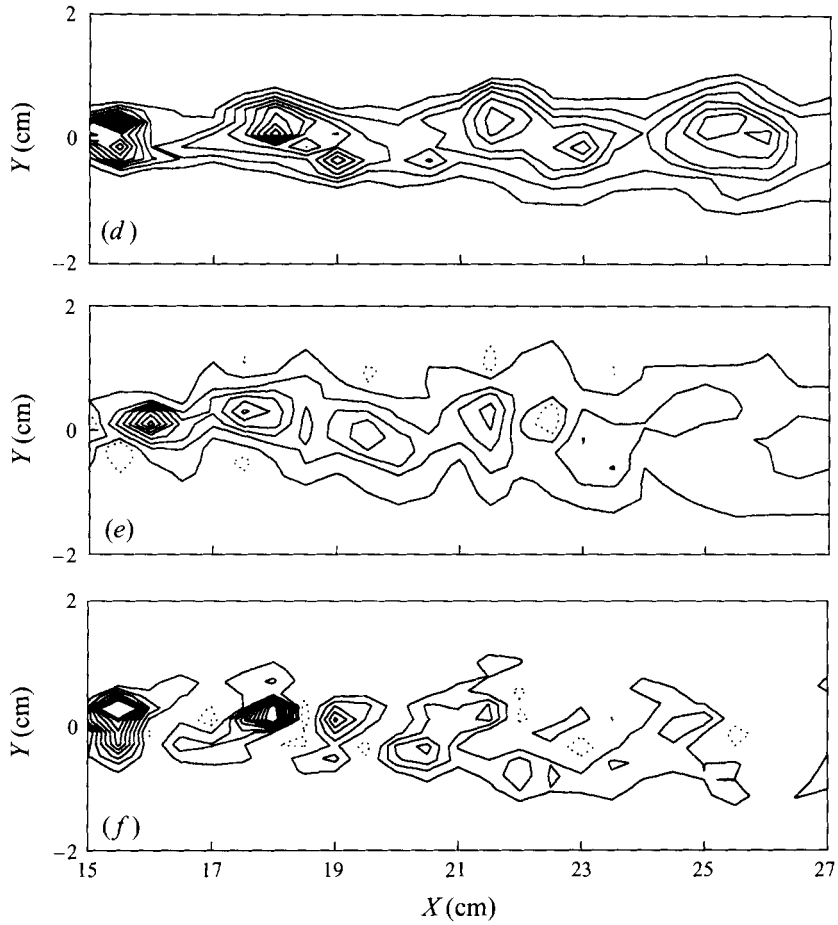

FIGURE 24. Phase-averaged streamwise velocity and Reynolds stress contours at phase 1 in the downstream domain through a rib plane (Z = 0.25 cm). (*a*) $\langle U\rangle/U_0$, lowest level = 1.6, increment = 0.1; (*b*) $\langle u'^2\rangle/U_0^2$, lowest level = 0.01, increment = 0.01; (*c*) $\langle v'^2\rangle/U_0^2$, lowest level = 0.005, increment = 0.015; (*d*) $\langle w'^2\rangle/U_0^2$, lowest level = 0.008, increment = 0.005; (*e*) $\langle u'v'\rangle/U_0^2$, lowest level = $\pm$0.004, increment = $\pm$0.015; (*f*) $\langle u'w'\rangle/U_0^2$, lowest level = $\pm$0.003, increment = $\pm$0.004.

plane $\langle w'^2\rangle$ (figure 22*a*). Note that the levels of $\langle w'^2\rangle$ are generally higher on the negative-Z side in both the roller core plane and mid-braid plane and that significant $\langle w'^2\rangle$ and $\langle u'w'\rangle$ are absent between the ribs (i.e. in between-rib planes as was indicated above).

Longitudinal (X, Y-plane) cuts through the data in the downstream domain (region of spanwise vortex pairing) are presented for the rib plane (Z = 0.25 cm) in figure 24(*a–f*). The $\langle U\rangle$ contours (figure 24*a*) still show a pinched effect, although it is less severe than in the near-field region. Also, an increase in mixing layer thickness is apparent around $X \approx 20$ cm, where the two spanwise vortices amalgamate. The qualitative behaviour of the three normal stresses (figure 24*b–d*) is comparable to that for the near-field region with local peaks coinciding with the locations of the spanwise rollers. The primary shear stress ($\langle u'v'\rangle$, figure 24*e*) is now almost all negative and is also generally higher in the regions of the spanwise rollers, although the peaks are not as pronounced as in the normal stress distributions. The secondary shear stress

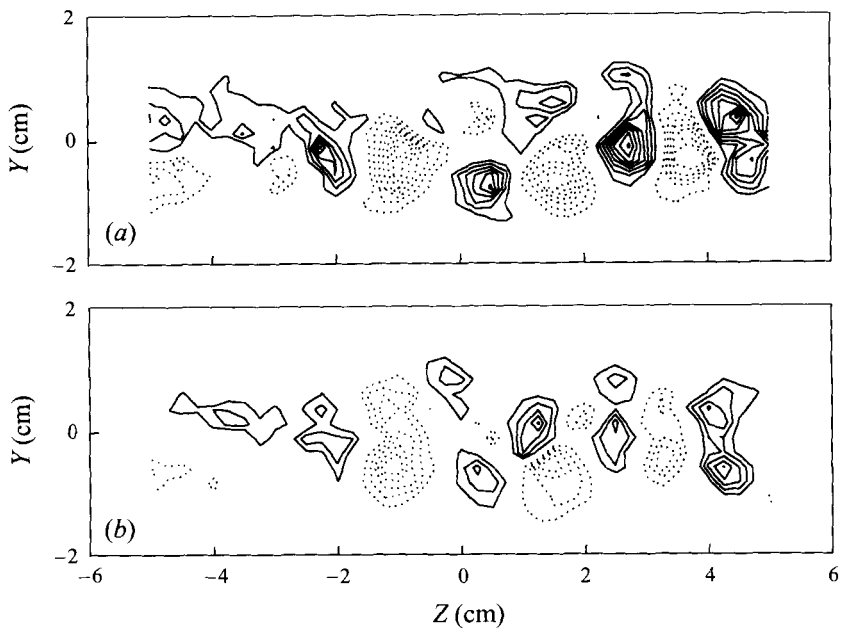

FIGURE 25. Cross-stream plane phase-averaged secondary shear stress ($\langle u'w'\langle/U_0{}^2$) contours at phase 1; lowest level = $\pm$0.003, increment = $\pm$0.002. (*a*) roller core plane (X = 22 cm); (*b*) mid-braid plane (X = 23.5 cm).

($\langle u'w'\rangle$, figure 24*f*) behaviour is similar to that in the near-field region, with positive levels in the braid regions and negative levels in the primary roller cores. In this subdomain, the magnitude of all stress component peaks within the spanwise vortex regions tends to decrease with streamwise distance. The streamwise development of the peak (time-averaged) Reynolds stresses, together with that of the periodic and random contributions, is presented and discussed below in §4.4.2.

The corresponding contours in the between-rib planes have not been included since in this region, the phase-averaged streamwise velocity, normal stresses and primary shear stress are qualitatively similar to those in the rib plane. The secondary shear stress is virtually negligible in the between-rib planes as can be seen in the roller core plane (X = 22 cm) and mid-braid plane (X = 23.5 cm) contours shown in figure 25(*a*) and 25(*b*), respectively. Comparison of figures 25(*b*) and 17(*d*) shows a strong correlation between the braid region secondary shear stress peaks and opposite-signed peaks of streamwise vorticity. This is clearly not the case for the roller core plane streamwise vorticity (compare figures 25*a* and 17*c*). In fact, the mid-braid plane and roller core plane secondary shear stress contours look remarkably similar. These results help explain the strong relationship between $\overline{u'w'}$ and the mean (time-averaged) streamwise vorticity found by Bell & Mehta (1992), since in the downstream region, the main contribution to the mean streamwise vorticity comes from the rib vortices (see §4.2).

As noted above, the phase-averaged total Reynolds stress contours presented here contain periodic as well as random contributions. At least in the near-field region, the periodic contribution (due to the passage of the spanwise rollers) would be expected to dominate and so it is perhaps not too surprising to see the maximum phase-averaged (total) stress levels in the spanwise vortex cores. However, the present

measurements showed that even the phase-random Reynolds stresses (not presented here) were generally higher in the spanwise rollers, in agreement with some previous observations. Tung (1992) reported higher levels of phase-random Reynolds stress in the spanwise core regions and a strong correlation between locations of peaks in $\langle w''^2\rangle$ and $\langle u''w''\rangle$ and those of the streamwise vortices. In cross-stream plane cuts in the present study, local peaks in $\langle w''^2\rangle$ and $\langle u''w''\rangle$ were generally observed at the locations of the streamwise vortices, with the peaks higher in the roller core planes than in the mid-braid planes. Nygaard & Glezer (1991) also observed relatively high values of 'true' r.m.s. streamwise velocity fluctuations (computed relative to each individual data record and then ensemble-averaged) in the spanwise rollers and large spanwise variations within the spanwise vortex cores and in the braid regions.

The higher levels of phase-random stress in the spanwise vortex core regions are probably a direct result of the mean shear ($\partial\langle U\rangle/\partial Y$) being higher in these regions (as seen in figure 21*a*, for example), thus leading to more production. Peaks of $\langle w''^2\rangle$ are generated in the regions of streamwise vorticity since these are regions where large spatial gradients of $\langle W\rangle$ are produced. As shown previously by Bell & Mehta (1992), the secondary shear stress $\overline{u'w'}$ is extremely well correlated with the mean streamwise vorticity since the main velocity gradient producing it ($\partial U/\partial Z$) is a maximum at the streamwise vortex core location. Peaks of $\langle u''w''\rangle$ in the present data must be generated through the same production mechanisms. The peaks of $\langle w''^2\rangle$ and $\langle u''w''\rangle$ are generally higher in the roller core planes than in the mid-braid planes mainly because the combination of stresses and velocity gradients which produce $\langle w''^2\rangle$ and $\langle u''w''\rangle$ are higher in the roller core planes. For example, dominant production terms for $\langle w''^2\rangle$ and $\langle u''w''\rangle$, respectively include $\langle v''w''\rangle\partial\langle W\rangle/\partial Y$ and $\langle w''^2\rangle\partial\langle U\rangle/\partial Z$.

As noted above in §3.3.2, the phase-averaged streamwise vorticity decays with streamwise distance, but the rate of decay appears to be higher on the negative-Z side. The phase-averaged Reynolds stresses discussed above also show a bias in the cross-stream planes such that they are generally higher on the negative-Z side. In addition, the coherence, as defined in equation (3.3), was found to be lower on the negative-Z side. This implies that transition (indicated by the increasing random velocity components) in the free-shear layer is probably occurring earlier on that side – note that the 'naturally occurring' disturbances in the incoming flow are not necessarily spanwise uniform. Among other effects, the faster transition would lead to more comparable levels of $\langle v''^2\rangle$ and $\langle w''^2\rangle$, and hence $\langle v'^2\rangle$ and $\langle w'^2\rangle$, on that side. Bell & Mehta (1992) showed how the anisotropy parameter $(\overline{v'^2} - \overline{w'^2})$ was related to the production or 'maintenance' of streamwise vorticity. In essence, if the anisotropy parameter is zero, then there will be no contribution from this term and the streamwise vorticity will decay faster. Hence, the faster decay rate of $\langle\Omega_x\rangle$ on the negative-Z side in the present study is probably due to the lower levels of the anisotropy parameter ($\langle v'^2\rangle - \langle w'^2\rangle$) on that side.

4. Further discussion

4.1. *Origin and evolution of streamwise vorticity*

The fact that significant streamwise vorticity is not measured in the very near-field region ($1 < X < 3$ cm) of the present mixing layer (figure 10*a–d*), supports the view that the appearance of streamwise vorticity further downstream is due to an amplification of very weak incoming disturbances – it is not just a simple case of relatively strong streamwise vorticity being fed-in directly from the boundary layers.

Moreover, Moser & Rogers (1991) indicated that even initial disturbance circulations high enough to cause transition by the second pairing of their simulations could be imperceptible in splitter-plate boundary layer measurements. In this study, noticeable amplification occurs as soon as the first spanwise vortex starts to roll up and stretching of the (upstream) braid is achieved.

Most of the previous experimental studies have also reported the relatively early appearance of the streamwise vorticity. Lasheras *et al.* (1986) found that, depending on the intensity of the upstream disturbances, streamwise vortices could be observed as early as the location of the first spanwise vortex. Based on the spectral content of spanwise velocity fluctuations, Huang & Ho (1990) concluded that the streamwise vortices 'develop together with the spanwise structures from the very beginning of the mixing layer'. Nygaard & Glezer (1991) also observed that the secondary structure formed upstream of the first spanwise vortex roller when they induced streamwise vortex formation by employing a mosaic of surface film heaters. In contrast, Tung (1992) reported that rib vortices first appeared in a forced mixing layer only when the spanwise rollers paired. This was in spite of the fact that the rib vortices seemed to be triggered by isolated disturbances on the splitter plate. This may be indicative of excessive two-dimensional forcing in his study. The effects of forcing on the mixing layer three-dimensionality in the present study are discussed below in §4.3.

The ratio of the initial spanwise to streamwise (Kelvin–Helmholtz) wavelength is about 1.3 in the present study. On re-examining the mean streamwise vorticity measurements of Bell & Mehta (1992), and applying what we now know about the near-field behaviour, it was found that their ratio was also about 1.3. The stability analysis of Pierrehumbert & Widnall (1982) suggested that the mixing layer will amplify spanwise disturbances more-or-less equally over a broad range of wavelengths, with the most-amplified wavelength being about 2/3 of the Kelvin–Helmholtz wavelength. A linear analysis by Rogers & Moser (1993) also showed that a ratio of about 2/3 produced the largest long-term growth in a pairing mixing layer. Several previous experimental studies (Konrad 1976; Breidenthal 1981; Jimenez 1983; Jimenez *et al.* 1985; Bernal & Roshko 1986; Lasheras *et al.* 1986, Huang & Ho 1990; Tung 1992) have all reported that the initial average wavelength is of the same order of magnitude as the Kelvin–Helmholtz wavelength. So the balance of evidence suggests that, given a broad range of initial disturbance wavelengths, the one that is comparable to the Kelvin–Helmholtz wavelength will most likely be amplified. Of course, as shown by Lasheras & Choi (1988) and Nygaard & Glezer (1991), in the presence of relatively strong external forcing, the streamwise structures can be locked over a much wider range of wavelengths.

The above observation regarding the spanwise wavelength certainly does not mean that the newly formed streamwise vortex structure is fully independent of the initial conditions. As demonstrated by Jimenez (1983) and Bernal & Roshko (1986), the spanwise locations at which the streamwise vortices first appeared could be altered by changing the flow conditions on the splitter plate. Moreover, Bell & Mehta (1992) showed that the locations of their initial 'clusters' of mean streamwise vorticity were at least weakly correlated with those of weak disturbances in the initial boundary layers. It therefore appears that, in practice, although the initial average spanwise wavelength will tend to be of the *same order* as the Kelvin–Helmholtz wavelength, the exact initial locations, and hence spacing, of the streamwise vortices will be determined by the details of the initial disturbance environment. Furthermore, the details of the generated array of streamwise vortices (size and strength) will also be dependent on the initial conditions. As observed in the present results (figure

10), the initial streamwise vortex array (and its subsequent development) will not generally be spanwise-uniform in these spatially developing mixing layers since the initial disturbance environment is not expected to be uniform.

The present results also show that there is not much effect of the spanwise vortex pairing on the structure of the surviving rib vortices. This was also observed in the spatial simulation results of Buell & Mansour (1989). The fact that the spanwise spacing of the ribs did not increase through the first pairing is not too surprising since a spanwise scale change is not always observed after every spanwise vortex pairing (Breidenthal 1981; Lasheras *et al.* 1986; Lasheras & Choi 1988; Bell & Mehta 1992). In the previous time-averaged measurements in a similar, but unforced, mixing layer (Bell & Mehta 1992), the first increase in spacing was not observed until $X \approx$ 50 cm, estimated to be after at least two spanwise vortex pairings. LeBoeuf & Mehta (1995*a*) showed recently that the first increase in spacing occurred during the third pairing in their forced mixing layer generated in the same facility. So the balance of experimental evidence suggests that the details of a scale change are a strong function of the initial disturbance environment, thus confirming the observations of Rogers & Moser (1993) from their direct numerical simulation results.

The present results clearly support the notion that the details of the initial streamwise vortex structure and its subsequent evolution seem to be more dependent on the initial conditions than on the dynamics of the mixing layer.

4.2. *Composition of time-averaged 'structures'*

Bell & Mehta (1992) showed that the mean streamwise vorticity distributions, obtained from time-averaged secondary velocities, tend to look different in the near-field region than those downstream of the estimated first spanwise vortex pairing location. They found that the clusters of mean streamwise vorticity, essentially consisting of the three-tier arrangement, observed in the near-field region 're-aligned' into a single row of counter-rotating pairs further downstream ($X \geqslant 37$ cm). As discussed above in §3.3.2, the present results show that the reason for this difference is that the relative contribution of the streamwise vorticity in the roller core planes (both due to the kinking of the rollers and that of the ribs) decreases with downstream distance. The relationship between the phase-averaged and time-averaged structure can be demonstrated by comparing roller core plane and mid-braid plane phase-averaged streamwise vorticity to the mean streamwise vorticity at the same station.

For the near-field region ($X = 12$ cm), phase-averaged streamwise vorticity contours through a roller core plane (phase 1) and mid-braid plane (phase 5) are shown in figure 26(*a*) and 26(*b*), respectively and the resulting time-averaged vorticity distribution is presented in figure 26(*c*). It is clear that the time-averaged picture is dominated by the stronger three-tier distribution in the roller core planes. The effect of the rib vortices in the averaging is mainly to weaken the opposite-signed (central) core vorticity due to the kinked primary rollers.

The corresponding phase-averaged streamwise vorticity contours through a roller core plane (phase 16) and mid-braid plane (phase 8) at $X = 25$ cm, downstream of the spanwise vortex pairing, are presented in figure 27(*a*) and 27(*b*), respectively, with the time-averaged result shown in figure 27(*c*). In this region, the time-averaged vorticity distribution looks very similar to that in the mid-braid plane which contains higher streamwise vorticity levels than those in the roller core plane. The weaker opposite-signed core vorticity does not contribute significantly to the averaging process and somewhat elongated (in the vertical, Y, direction) structures, arranged in a single row of counter-rotating pairs, appear in the time-averaged distribution. As shown

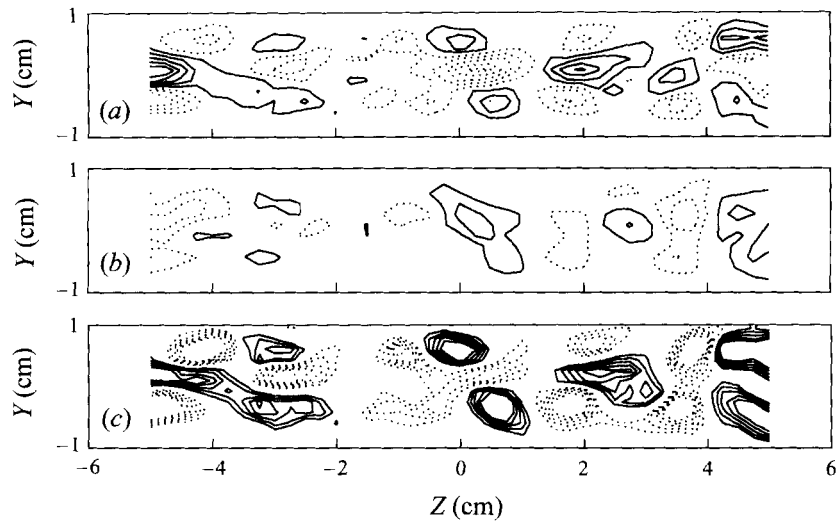

FIGURE 26. Cross-stream plane phase- and time-averaged streamwise vorticity contours at X = 12 cm; lowest level = ± 0.2, increment = ± 0.3. (*a*) Roller core plane (phase 1); (*b*) mid-braid plane; (*c*) time-averaged.

by Bell & Mehta (1992), the single row arrangement is retained further downstream, although the peak mean streamwise vorticity of the structures decays and the spacing between them increases in a stepwise fashion.

4.3. *Effects of acoustic forcing on streamwise vorticity*

The effects of two-dimensional forcing on the three-dimensional structure are, of course, always a concern when the sole purpose of the forcing is to phase-lock the mixing layer development. It is conceivable that the three-dimensionality of a mixing layer could be suppressed if the (two-dimensional) forcing is too strong. In the present study, the forcing amplitude was set to the absolute minimum level which still adequately phase-locked the roll-up and pairing of the spanwise rollers.

In order to assess the effects of forcing, time-averaged data were also obtained with the acoustic forcing turned off, but with all other conditions maintained exactly the same. At a given station, the mean streamwise vorticity thus obtained in this 'unforced' mixing layer can then be compared directly to the vorticity averaged over all phases in the forced case. The mean streamwise vorticity contours with and without forcing at X = 8, 20 and 27 cm, representing stations before, during and after pairing, are compared in figure 28(*a*)–28(*c*), respectively. On the whole, and considering the fact that the two data sets were obtained completely independently, the distributions compare quite well at all streamwise locations, although there are some detailed differences. In general, the number of measured streamwise vortical 'structures' is the same in both mixing layers, but the vorticity levels in the forced case are slightly higher – compare the structures in the forced and unforced layers between Z = 0 and 5 cm in figure 28(*b*), for example. So, at least as far as the three-dimensional (mean) structure of the mixing layer is concerned, the acoustic forcing does not appear to have affected it significantly. Further comparisons of some of the global properties of the forced and unforced mixing layers are given below in §4.4.

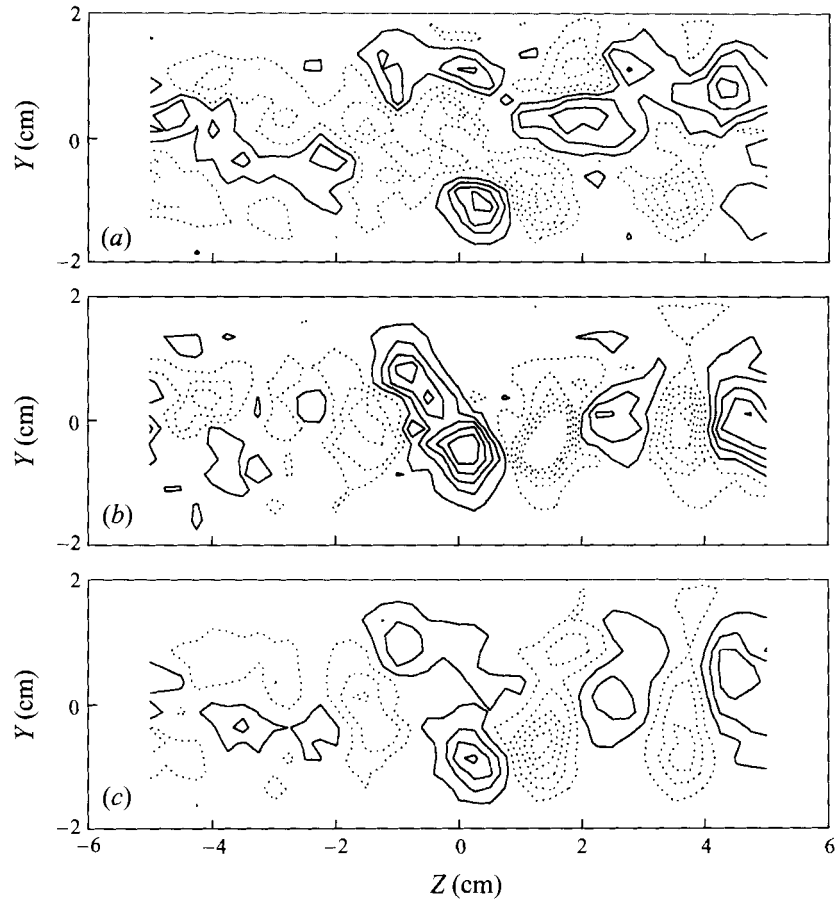

FIGURE 27. Cross-stream plane phase- and time-averaged streamwise vorticity contours at X = 25 cm; lowest level = ± 0.04, increment = ± 0.08. (*a*) Roller core plane (phase 16); (*b*) mid-braid plane (phase 8); (*c*) time-averaged.

4.4. *Streamwise development of global properties*

4.4.1. *Streamwise and spanwise vortex properties*

The properties of a vortex are best studied by examining its maximum vorticity level and circulation. The streamwise vorticity and circulation for the structures measured in the present study were evaluated as described above in §2.

The streamwise development of the absolute maximum mean streamwise vorticity, averaged over all (positive and negative) structures identified at a given station, is plotted in figure 29(*a*) for three cases. In addition to the forced and unforced cases, both time-averaged, the maximum vorticity at a given phase (phase 1) for the forced case is also shown. Overall, the three cases exhibit similar trends whereby the maximum vorticity increases in the near field, achieves a maximum in the region $X \approx 5$–10 cm, and then decreases gradually further downstream. So the maximum streamwise vorticity is achieved in a region between the location of the initial spanwise vortex roll-up and that of the first pairing, implying that some amplification of the streamwise vorticity occurs in the very near-field region. The forced data also show another smaller rise at $X \approx 15$ cm, the approximate location where pairing of the spanwise vortices starts to occur. This local intensification of streamwise vorticity in

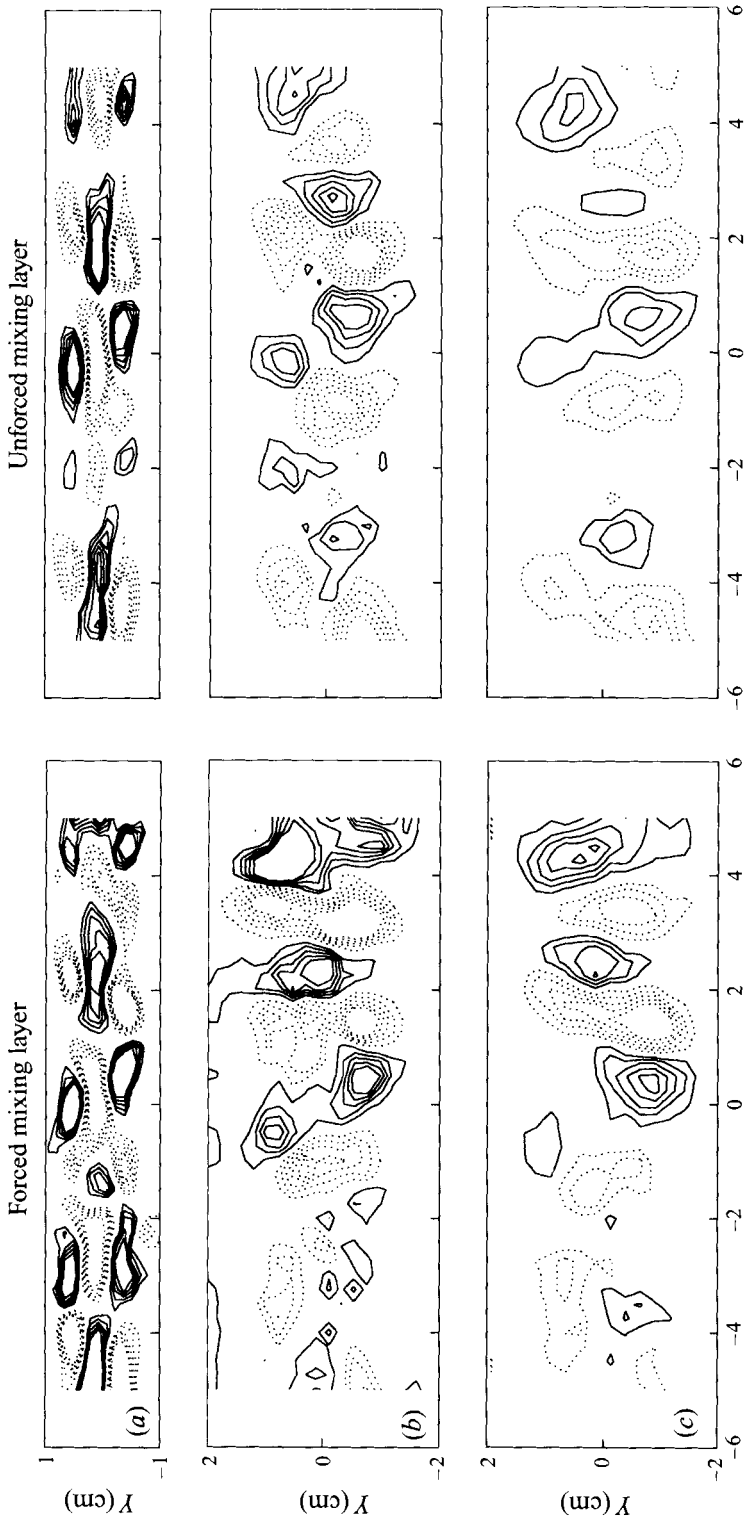

FIGURE 28. Comparison of time-averaged streamwise vorticity Ω_x/U_0, (cm^{-1}) contours for forced and unforced cases. (*a*) X = 8 cm, lowest level = $\pm$0.1, increment = $\pm$0.05; (*b*) X = 20 cm, lowest level = $\pm$0.05, increment = $\pm$0.05; (*c*) X = 27 cm, lowest level = $\pm$0.05, increment = $\pm$0.05.

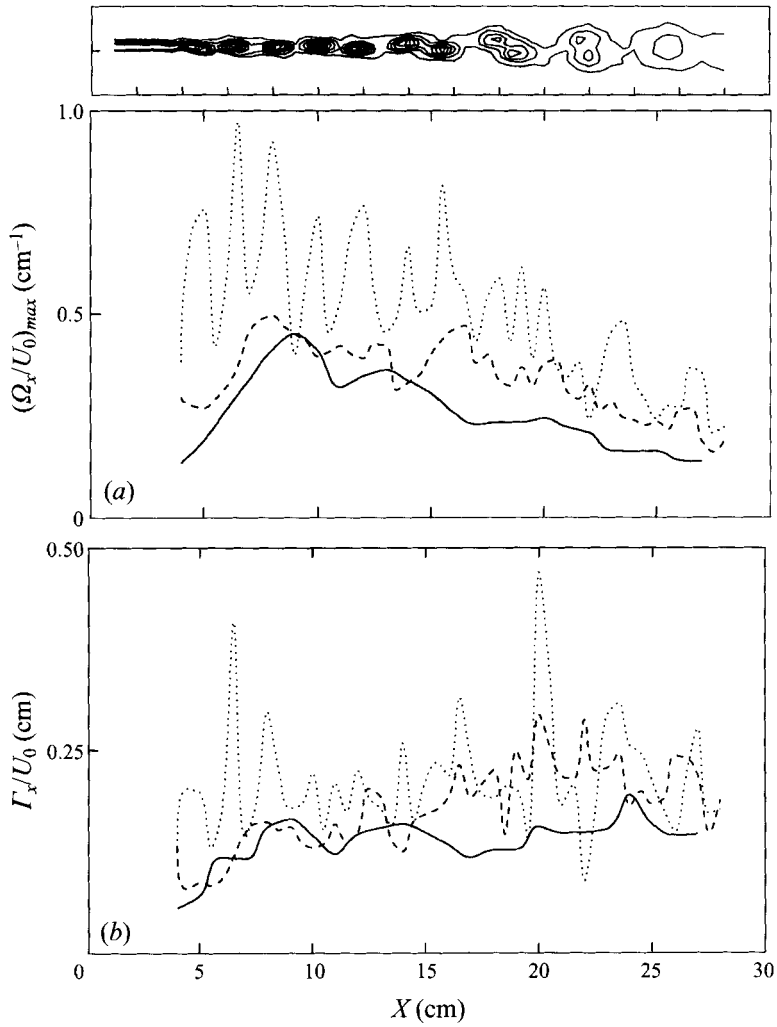

FIGURE 29. Streamwise development of phase- and time-averaged streamwise vortex properties. Unforced (time-averaged): ———, forced (time-averaged): - - - -, forced (phase-averaged): · · · · · ·. (*a*) Peak streamwise vorticity; (*b*) Average streamwise vortex circulation.

the perishing braid region (between the two pairing rollers) was also reported by Tung (1992). On examining the phase-averaged spanwise vorticity contours (figure 6) it became apparent that this is the region where the row of spanwise rollers first becomes displaced in the vertical (Y) direction, in preparation for the pairing, such that the leading vortex (within the pair) moves downwards. As a result, the braid region between them becomes more aligned with the mean flow and a higher contribution to the streamwise vorticity is obtained.

On comparing the distribution with the superimposed spanwise vorticity plot, it is apparent that the local extrema coincide with features of the mixing layer structure. In the near-field region ($X < 17$ cm), the maxima and minima coincide with the spanwise roller and braid locations, respectively. This confirms the notion, developed from the streamwise vorticity contours (§3.3), that in the near-field region, the maximum levels of streamwise vorticity occur in the spanwise vortex core regions (roller core planes).

This is mainly due to the fact that the rib vortices are more aligned with the mean flow in the roller core planes and there is also a strong contribution due to the kinking of the spanwise rollers. In the region of roller pairing ($17 < X < 21$ cm), the three peaks (of comparable amplitude) are located at the roller core planes of the two pairing rollers and at the location of the downstream surviving braid. Downstream of the pairing region ($X > 21$ cm), the maxima and minima coincide with the braid and roller core locations, respectively. So, in contrast to the near-field region, the rib streamwise vorticity in the braids is now stronger than the rib contribution in the roller core plane. As was pointed out in §3.3.2, this change occurs because the ends of the ribs (wrapped around the roller) are now tilted in the spanwise direction, thus making their contribution to the roller core plane streamwise vorticity smaller. The maximum levels of phase-averaged streamwise vorticity measured in the present investigation are comparable to those reported by Tung (1992).

In comparing the (time-averaged) results for the forced and unforced layers, the maximum streamwise vorticity levels in the forced mixing layer are somewhat higher than those measured in the unforced case, especially in the region beyond $X \approx 15$ cm – this bias was also apparent in the comparison of the mean streamwise vorticity contours (figure 28). However, by the end of the measurement domain, the maximum mean streamwise vorticity levels in the two cases are comparable, implying that the higher levels are an artifact of the forcing, and hence the mixing layer dynamics, and not due to a change in the initial or operating conditions. The behaviour of the unforced maximum mean streamwise vorticity agrees well with the previous measurements of Bell & Mehta (1992).

The streamwise development of forced and unforced time-averaged and forced phase-averaged absolute circulation (averaged over the individual streamwise structures) is plotted in figure 29(*b*). The average circulation is approximately constant in all three cases. As with the vorticity, in the near-field region, local peaks in the phase-averaged case occur at locations of the spanwise rollers while those in the downstream region are coincident with the braid regions. Furthermore, the levels in the (time-averaged) forced case are higher than those in the unforced case downstream of $X \approx 15$ cm. And again, the circulation levels for the forced and unforced cases become comparable by the end of the measurement domain. The behaviour and levels of the average circulation in the unforced case are similar to those measured earlier (Bell & Mehta 1992).

The fact that the peak mean streamwise vorticity and average streamwise circulation levels in the forced and unforced cases are comparable in the near-field region and higher in the forced case downstream of the pairing imply that the two-dimensional forcing certainly has not suppressed the three-dimensionality. The differences in the vicinity of the pairing are directly attributable to the forcing. At a given streamwise location, the orientation of each spanwise vortex passing by is fixed in the forced case, but tends to 'jitter' in the unforced case. This should not affect the (time-averaged) streamwise vorticity measurements in the near-field region (prior to pairing) since the orientation of the rollers is not critical. However, in the region of pairing, for every cycle, the fixed orientation of the (forced) pair of merging spanwise rollers will make a higher contribution to the streamwise vorticity than in the unforced case where the orientation of each pair passing by can be very different, hence leading to a 'wash-out' effect.

The streamwise distribution of the spanwise vorticity and circulation (magnitudes) for a centreline ($Z = 0$) cut through the data at phase 1 is presented in figure 30. Using the spanwise vorticity contours, each identified spanwise vortex was first 'boxed'

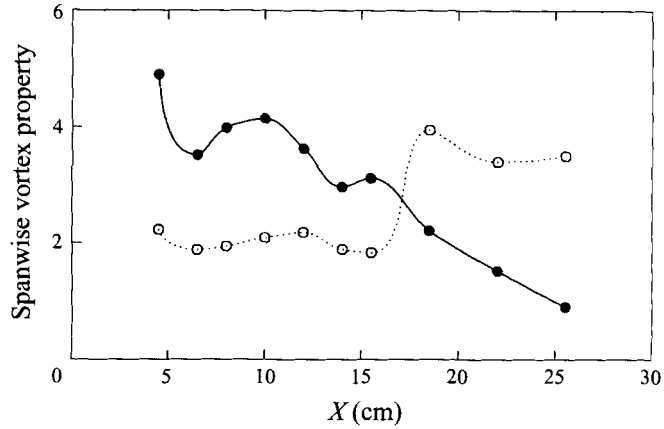

FIGURE 30. Streamwise development of phase-averaged spanwise vortex property magnitudes along the centreline ($Z = 0$). Peak spanwise vorticity $[(\Omega_z/U_0)_{max}\ (\mathrm{cm}^{-1})]$: •; spanwise circulation $[(\Gamma_z/U_0)\ (\mathrm{cm})]$: ○.

(visually). The maximum vorticity and circulation within each box were then evaluated separately and plotted based on the streamwise location of the peak vorticity of each roller. The maximum spanwise vorticity generally shows a decreasing trend, except for temporary increases at $X \approx 10$ and 15 cm. It was remarked above in §3.3.2 that the change in the opposite-signed streamwise vorticity levels in the roller core planes before and after pairing (i.e. a relative reduction of the primary roller contribution to Ω_x) may be partly attributable to the change in peak vorticity levels. A comparison of the relative strengths of the maximum (phase-averaged) streamwise vorticity in the near-field ($X \approx 5$ to 15 cm) ribs (corresponding to dips in the $\langle\Omega_x\rangle$ distribution in figure 29*a*) and the maximum spanwise vorticity of the near-field rollers (measured within the rollers) gives a ratio of about 10–15%. In the first shed (detached) spanwise roller (i.e. the second roller at $X \approx 7$ cm), the ratio of peak streamwise to spanwise vorticity is about 30%. This ratio of peak streamwise to spanwise phase-averaged vorticity increases from 30% at $X \approx 7$ cm to about 35% at $X \approx 27$ cm. This suggests that it is also the change in relative strengths of the streamwise and spanwise vorticity that leads to a smaller contribution due to kinking of the roller. The present results are consistent with the estimate of Bell & Mehta (1992) of the streamwise to spanwise vorticity ratio of about 30% based upon time-averaged measurements in a similar mixing layer.

The phase-averaged spanwise circulation is approximately constant up to $X \approx$ 15 cm. In this region, the average rib circulation (corresponding to dips in the phase-averaged distribution in figure 29*b*) is equivalent to about 5–10% of the spanwise circulation. However, the average roller core plane circulation (peaks in figure 29*b*) is equivalent to almost 20% of the spanwise circulation. At $X \approx 15$ cm, the spanwise circulation rises sharply and nearly doubles as a result of the spanwise vortex pairing. Consequently, the ratio of streamwise (rib) to spanwise circulation drops to approximately 3% in the far-field region of the domain ($X > 20$ cm). In comparison, Bell & Mehta (1992) reported an estimated near-field circulation ratio of about 10%, based on their time-averaged measurements and Rogers & Moser (1992) investigated circulation ratios ranging from 0.5% to 10%.

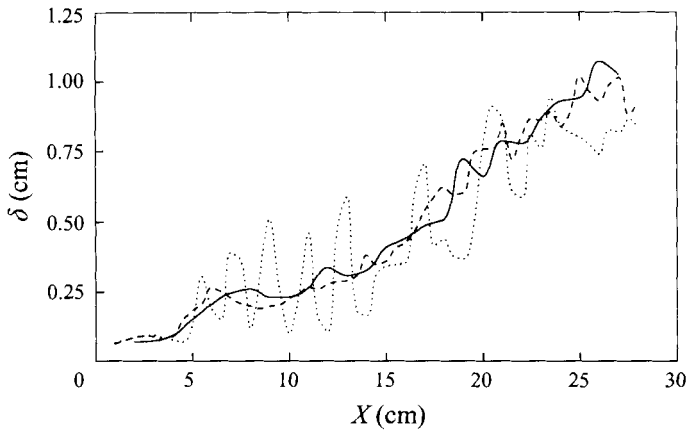

FIGURE 31. Streamwise development of phase- and time-averaged mixing layer thickness. Unforced (time-averaged): ——, forced (time-averaged): - - - -, forced (phase-averaged): · · · · · ·.

4.4.2. *Growth rate and peak Reynolds stresses*

As shown above in §3.4, relatively large spanwise variations in the Reynolds stress distributions were observed due to the presence of the secondary streamwise vortical structure. Therefore, in order to obtain a more accurate representation of the behaviour of some of the global properties of this mixing layer, such as the thickness and peak Reynolds stresses, a spanwise averaging technique was applied to the phase-averaged and time-averaged data. At a given streamwise location, the spanwise-averaged quantities were evaluated by dividing the measurements obtained on the cross-stream (Y,Z)-plane grid into individual Y-wise profiles along the span of the mixing layer. The mixing layer properties for each profile were then computed in the traditional manner. And finally, the profile-specific properties were algebraically averaged over all 41 spanwise positions, giving a single value of each quantity at each streamwise location. Further details of the averaging technique and its implications for three-dimensional mixing layers were reported by Bell, Plesniak & Mehta (1992).

Following Townsend (1976), the mixing layer thickness, δ, is defined by fitting the mean streamwise velocity data to an error function profile shape:

$$U^* = [1 + \mathrm{erf}(\zeta)]/2, \tag{4.1}$$

where $U^* = (U - U_2)/U_0$, $U_0 = U_1 - U_2$, the free-stream velocity difference, and ζ is the normalized Y-coordinate:

$$\zeta = (Y - Y_0)/\delta. \tag{4.2}$$

Values of δ and the mixing layer centreline, Y_0, were determined by optimizing the error function fit.

The streamwise development of the spanwise-averaged mixing-layer thickness (based on the time-averaged data) for the forced and unforced cases is shown in figure 31. Also included in this figure is the growth of the forced layer along the centreline ($Z = 0$) for phase 1. As the phase-averaged streamwise velocity contours (figure 21*a* and 24*a*) implied, the mixing layer thickness (at a given phase) varies significantly with streamwise distance, with minima achieved in the spanwise core regions and maxima within the braids.

Once again, the distributions for the forced and unforced (time-averaged) cases agree remarkably well, implying that the forcing did not affect the overall structure

and (spanwise-averaged) growth rate of the mixing layer significantly. Initially ($X <$ 5 cm), both mixing layers grow very slowly as the two boundary layers start to merge. However, once the Kelvin–Helmholtz instability sets in and the first roll-up occurs ($X \approx 5$ cm), a rapid growth is observed in both cases. Downstream of the roll-up ($X \approx 8$ to 15 cm), a region of slower growth is apparent in both cases since growth is being achieved only through entrainment by the spanwise rollers themselves. Note that the roll-up process occurs over a longer streamwise distance in the unforced case, as would be expected since in this case it occurs more randomly in space and time. Both mixing layers grow more rapidly in the region, $X \approx 15$ to 25 cm, where the first spanwise vortex pairing is occurring. Once again, downstream of $X \approx 25$ cm, the forced mixing layer growth rate seems to decrease since the pairing process is complete, whereas that of the unforced case is maintained because of the randomness in the pairing location. The trends for the forced and unforced mixing layer growth observed here are similar to those reported earlier by Huang & Ho (1990) and Tung (1992), especially if only centreline ($Z = 0$) data are plotted as in their studies; the spanwise averaging employed here tends to 'wash-out' some of the differences between the forced and unforced layers.

The streamwise evolution of the spanwise-averaged peak Reynolds stresses (time-averaged) for the forced and unforced cases is compared in figure 32(*a–d*). Overall, the distributions for the forced and unforced cases exhibit very similar qualitative trends, except that the local peaks in the forced case are typically higher due to the phase-locking. The vertical component ($\overline{v'^2}_{max}$) exhibits a single peak just downstream of the first spanwise roll-up ($X \approx 5$ cm). The streamwise component ($\overline{u'^2}_{max}$) and the primary shear stress ($\overline{u'v'}_{max}$) distributions contain two more peaks in addition, one at $X \approx 10$ cm and the other at $X \approx 15$–20 cm. The maximum spanwise normal stress ($\overline{w'^2}_{max}$) distribution shows a broad peak at $X \approx$ 15-20 cm, although smaller (less distinct) ones are also apparent at $X \approx 5$ cm and $X \approx 10$ cm, especially in the forced case.

In terms of the forced versus unforced comparisons, the notable differences are that $\overline{u'^2}_{max}$ and $\overline{u'v'}_{max}$ are higher in the forced case at $X \approx 15$ cm. The spanwise component, $\overline{w'^2}_{max}$, is higher in the unforced case at $X \approx 10$ cm, implying that the three-dimensionality in the forced mixing layer is perhaps suppressed in this region. However, as shown in figure 29(*a*), the peak mean streamwise vorticity levels in this region are comparable for the forced and unforced cases. Perhaps the most surprising result is that the streamwise distribution of $\overline{v'^2}_{max}$, which would be expected to be affected most by the forcing, is almost the same in both cases. This is perhaps the strongest evidence against the forcing in the present study being too excessive.

In order to assess how the local peaks in the peak Reynolds stress distributions are generated, the time-averaged (total) stress was decomposed to give the periodic and random contributions (equation (3.2)). The streamwise development of the contributions (time- and spanwise-averaged) is presented in figure 33(*a–d*). The first peak in the total stresses occurs at $X \approx 5$ cm. This is obviously due to the formation of the initial spanwise roller which would contribute directly to u' and v', and hence, $u'v'$. Of course, this should show up as a strong periodic contribution, and it does, as evidenced in figure 33(*a–c*). Not surprisingly, the periodic contribution to w', due to the nominally two-dimensional spanwise rollers, is quite small in comparison. The second peak in the total stresses, at $X \approx 10$ cm, is also a result of a strong contribution from the periodic component. On examining the spanwise vorticity contours, it became apparent that the spanwise vortex was 'fully rolled-up' some distance downstream of the shedding point, in the region between $X = 5$ and 10 cm.

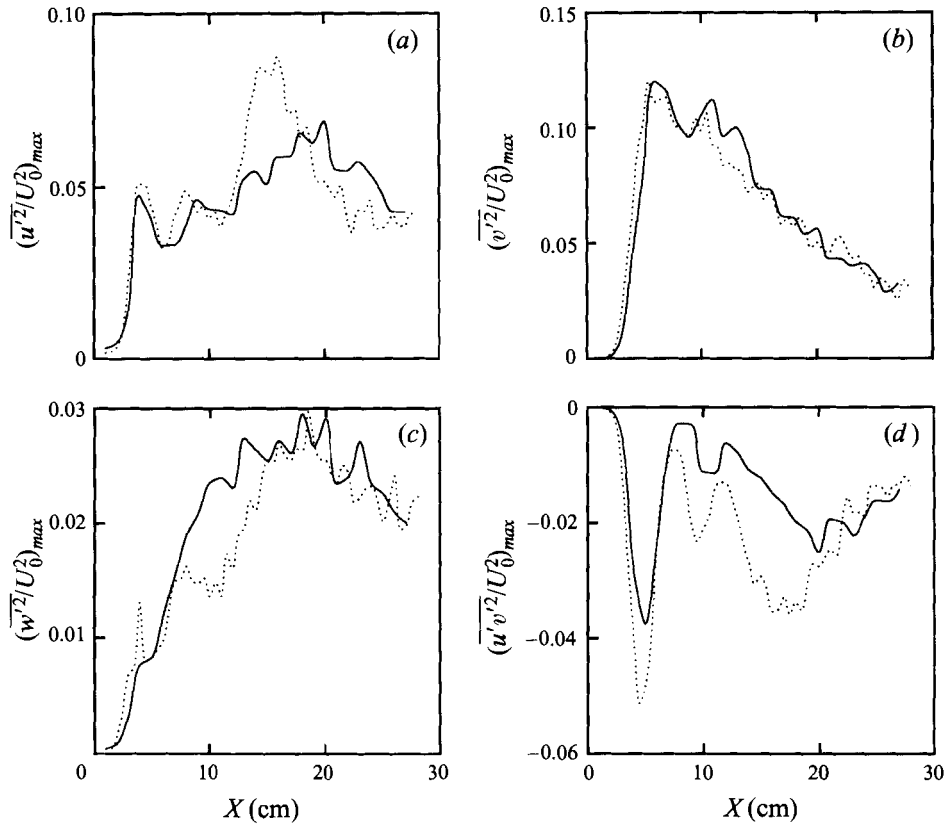

FIGURE 32. Streamwise development of time- and spanwise-averaged peak Reynolds stresses for the forced and unforced mixing layers. Forced: ·····, unforced: ———. (*a*) Streamwise normal stress; (*b*) cross-stream normal stress; (*c*) spanwise normal stress; (*d*) primary shear stress.

At that stage the spanwise vorticity within its core is maximized compared to its neighbours as shown in figure 30, and it is this roller that produces the second peak. The small second peak in $\overline{w'^2}_{max}$ at $X \approx 7$ cm corresponds to the highest peak in the periodic contribution. This periodic contribution to the spanwise component seems to be a result of the spanwise kinking of the roller. The high peak in $\overline{u'^2}_{max}$ at $X \approx 15$ cm is again due to a strong periodic contribution as seen in figure 33(*a*). The spanwise vorticity contours (figure 6*a*) show that this is the region where the spanwise vortices are displaced vertically, in preparation for the pairing sequence. As a result, the streamwise velocity ($\langle U \rangle$) contours in the (X, Y)-plane start to become inclined, as evidenced in figure 21(*a*). A local region of strong streamwise gradient ($\partial \langle U \rangle / \partial X$) is thus generated which will make a periodic contribution to the streamwise fluctuation. For all stresses in the downstream region ($X > 20$ cm), contributions of the random components increase relative to those of the periodic components as transition and loss of coherence in the mixing layer starts to occur.

5. Conclusions

An experimental investigation of the three-dimensional structure in the near-field region of a forced plane mixing layer has been completed. The initial spanwise vortex roll-up and first pairing were phase-locked using two-dimensional acoustic forcing.

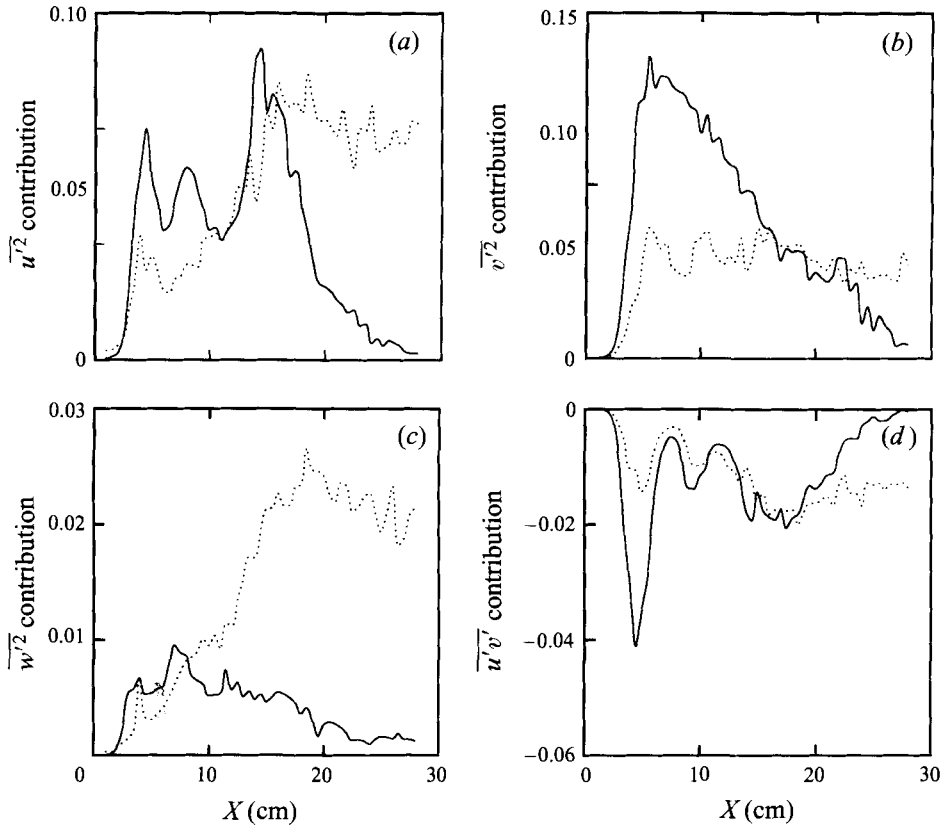

FIGURE 33. Streamwise development of time- and spanwise-averaged periodic and random contributions to the total Reynolds stress. Periodic contribution: ——, random contribution: ·····. (*a*) Streamwise normal stress contributions; (*b*) cross-stream normal stress contributions; (*c*) spanwise normal stress contributions; (*d*) primary shear stress contributions.

All three components of velocity were measured on a three-dimensional grid, thus enabling the evaluation of the phase-averaged vortical structure morphology, without invoking Taylor's hypothesis.

It was confirmed that the relative phase between the fundamental and subharmonic forcing signals determines the type of pairing interaction that will occur. The relative phase that gives a 'normal' (rolling-type) pairing interaction with maximum overall coherence was identified ($\beta_2 = 22.5°$) and set fixed throughout the present experiments. The forcing amplitude was set to the lowest level which still gave the desired coherence in the phase-locking. In order to ensure that the two-dimensional forcing was not affecting the three-dimensional structure significantly, several time-averaged quantities, such as the mean streamwise vorticity, peak Reynolds stress distributions and growth rates were compared for the forced and unforced mixing layers. On the whole, the two layers compared quite well although the peak mean streamwise vorticity and Reynolds stress levels were somewhat higher in the forced case. This is due to the localization of the spanwise vortex roll-up and pairing in the forced case which otherwise occurs randomly (in the absence of forcing). The present time-averaged measurements, especially those for the unforced case, compared well with those previously obtained by Bell & Mehta (1992) in a similar mixing layer

generated in the same wind tunnel. Furthermore, the maximum phase-averaged streamwise vorticity levels are comparable to those measured by Tung (1992).

The phase-averaged vorticity measurements confirm that relatively strong streamwise vorticity appears in mixing layers as a result of an amplification of small incoming disturbances – it is not just directly fed-in from the boundary layers. The streamwise vorticity is first observed in the form of ribs just upstream of where the first spanwise vortex is rolling up. At the same time, the first spanwise roller becomes kinked, thus also contributing to the streamwise vorticity. As a result, cross-stream cuts through the braid regions show the familiar row of counter-rotating streamwise vortex pairs while those through the spanwise rollers exhibit a three-tier distribution consisting of the rib vortices aligned vertically with an opposite-signed contribution from the roller between them. This type of behaviour and distribution are in agreement with previous observations in experiments and simulations (Tung 1992; Buell & Mansour 1989; Rogers & Moser 1992). The initial phase-averaged maximum streamwise vorticity in the ribs is equivalent to about 10–15% of the phase-averaged maximum spanwise vorticity and the average rib circulation is equivalent to about 5–15% of the spanwise vortex circulation. These values are more representative of the relative rib strength than those estimated by Bell & Mehta (1992) from their time-averaged measurements – a streamwise to spanwise ratio of approximately 30% for the initial vorticity and about 10% for the circulation. In the present study, after an initial amplification phase, the peak streamwise vorticity decreases with streamwise distance while the circulation remains more or less constant.

Because of the relatively strong contribution of the kinked rollers and the fact that the rib vortices are more aligned with the mean flow around the rollers, the highest levels of phase-averaged streamwise vorticity and circulation are observed in the spanwise vortex cores in the near-field region. The strong kinking of the spanwise rollers by the rib vortices was also observed in numerical simulations (Buell & Mansour 1989; Rogers & Moser 1992). However, the cups of relatively strong spanwise vorticity (also a result of the rib-induced effects) reported for the simulation results were not observed in the present measurements. This is particularly surprising since the initial rib circulation in the present experiments is comparable to that used in the temporal simulations of Rogers & Moser (1992).

The morphology of the surviving braid region rib vortices was not significantly affected by the spanwise vortex pairing. In particular, their spanwise spacing did not increase after the pairing. This result is consistent with previous time-averaged measurements (Bell & Mehta 1992) which showed that the first increase in spacing did not occur until $X \approx 50$ cm, well downstream of the present measurement domain and after an estimated two spanwise vortex pairings had occurred. In fact, some of our recent measurements in this forced mixing layer, but where the initial development and first *three* pairings were phase-locked, clearly showed that the first spanwise scale change occurred during the third roller pairing (Leboeuf & Mehta 1995*a*). The balance of evidence seems to support the findings of Rogers & Moser (1993) who suggested that the details of the spanwise scale change are dependent on the nature of the initial disturbance environment. The main effect noted in the post-pairing region is that the levels of streamwise vorticity in the roller core planes are reduced such that the highest levels are now found in the braid region. The smaller relative contribution due to kinking of the spanwise rollers is related to both a reduction in roller kinking and a faster rate of decay of the spanwise vorticity compared to that of the streamwise vorticity. The ribs make a smaller contribution in the roller planes because their ends are tilted in the spanwise direction. This change in the relative

contributions is the reason why, in the time-averaged measurements, the three-tier distribution observed in the near-field region soon 're-aligns' into a single row of mean streamwise vorticity (Bell & Mehta 1992).

Relatively high levels of phase-averaged total Reynolds stress are measured in the spanwise vortex cores. In the near-field region, most of the contribution is from the periodic component due to the passage of the spanwise vortex rollers. A greater contribution from the random component is obtained towards the end of the measurement domain as transition starts to occur within the mixing layer and as coherence of the large-scale structure decreases. A good correlation is observed between the locations of the streamwise vortices and those of local peaks in $\langle w'^2 \rangle$ and $\langle u'w' \rangle$.

The present results clearly show that a plane mixing layer originating from laminar boundary layers will develop a three-dimensional structure in the form of streamwise vorticity as soon as the Kelvin–Helmholtz instability generates spanwise vortex rollers. Although, in practice, the details of the streamwise vortical structures will be facility dependent, they will generally appear in the form of an array of counter-rotating vortex pairs. The present data are consistent with existing models of the secondary structure: rib vortices are formed in the braid region which wrap around the spanwise rollers (from the bottom of one roller to the top of the next). The streamwise vorticity, and its associated effects on the mixing layer properties, decays slowly with streamwise distance, although it should not be expected to persist into the fully developed region (Bell & Mehta 1990, 1992). This secondary structure therefore forms an integral and important part of the structural morphology of a transitioning mixing layer.

This work was performed in the Fluid Mechanics Laboratory (FML), NASA Ames Research Center and was supported by the Center for Turbulence Research, NASA Ames Research Center/Stanford University and Grant NCC-2-55 from the FML. We are grateful to Drs R. D. Moser and M. M. Rogers for many helpful discussions and also for reviewing a draft of this paper. We would like to thank Dr J. H. Watmuff for sharing his digital sine-wave generator design and also for many invaluable suggestions and useful discussions of this work.

REFERENCES

ASHURST, W. T. & MEIBURG, E. 1988 Three-Dimensional shear layers via vortex dynamics. *J. Fluid Mech.* **189**, 87–115.

BELL, J. H. & MEHTA, R. D. 1989 Design and calibration of the mixing layer wind tunnel. *JIAA Rep.* TR-89. Dept. of Aeronautics and Astronautics, Stanford University.

BELL, J. H. & MEHTA, R. D. 1990 Development of a two-stream mixing layer with tripped and untripped boundary layers. *AIAA J.* **28**, 2034–2042.

BELL, J. H. & MEHTA, R. D. 1992 Measurements of the streamwise vortical structures in a plane mixing layer. *J. Fluid Mech.* **239**, 213–248.

BELL, J. H., PLESNIAK, M. W. & MEHTA, R. D. 1992 Spanwise averaging of plane mixing layer properties. *AIAA J.* **30**, 835–837.

BERNAL, L. P. & ROSHKO, A. 1986 Streamwise vortex structure in plane mixing layers. *J. Fluid Mech.* **170**, 499–525.

BREIDENTHAL, R. 1981 Structure in turbulent mixing layers and wakes using a chemical reaction. *J. Fluid Mech.* **109**, 1–24.

BROWN, G. L. & ROSHKO, A. 1974 On density effects and large structure in turbulent mixing layers. *J. Fluid Mech.* **64**, 775–816.

BUELL, J. C. 1991 A hybrid numerical method for three-dimensional spatially-developing free-shear flows. *J. Comput. Phys.* **95**, 313–338.

BUELL, J. C. & MANSOUR, N. N. 1989 Asymmetric effects in three-dimensional spatially-developing mixing layers. In *Proc. Seventh Symp. Turbulent Shear Flows, Stanford University, August*, pp. 9.2.1–9.2.6.

HERNAN, M. A. & JIMENEZ, J. 1982 Computer analysis of a high-speed film of the plane mixing layer. *J. Fluid Mech.* **119**, 323–345.

HO, C.-M. & HUERRE, P. 1984 Perturbed free shear layers. *Ann. Rev. Fluid Mech.* **16**, 365–424.

HUANG, L.-S. & HO, C.-M. 1990 Small-scale transition in a plane mixing layer. *J. Fluid Mech.* **210**, 475–500.

INOUE, O. 1987 Three-dimensional vortex simulation of a plane mixing layer. In *Proc. Sixth Symp. on Turbulent Shear Flows, Toulouse, France, September 7-9*, pp. 22-1-1 to 22-1-6.

INOUE, O. 1992 Double-frequency forcing on spatially growing mixing layers. *J. Fluid Mech.* **234**, 553–581.

JIMENEZ, J. 1983 A spanwise structure in the plane mixing layer. *J. Fluid Mech.* **132**, 319–326.

JIMENEZ, J., COGOLLOS, M. & BERNAL, L. P. 1985 A perspective view of the plane mixing layer. *J. Fluid Mech.* **152**, 125–143.

KONRAD, J. H. 1976 An experimental investigation of mixing in two-dimensional turbulent shear flows with applications to diffusion-limited chemical reactions. *Project SQUID Tech. Rep.* CIT-8-PU; and PhD thesis, California Institute of Technology, 1977.

LASHERAS, J. C., CHO, J. S. & MAXWORTHY, T. 1986 On the origin and evolution of streamwise vortical structures in a plane, free shear layer. *J. Fluid Mech.* **172**, 231–258.

LASHERAS, J. C. & CHOI, H. 1988 Three-dimensional instability of a plane free shear layer: an experimental study of the formation and evolution of streamwise vortices. *J. Fluid Mech.* **189**, 53–86.

LEBOEUF, R. L. & MEHTA, R. D. 1993 Streamwise vortex meander in a plane mixing layer. *Phys. Fluids* A **5**, 1983–1991.

LEBOEUF, R. L. & MEHTA, R. D. 1995*a* Measurements of spanwise scale change in a forced mixing layer. *J. Fluid Mech.* **293**, 305–319.

LEBOEUF, R. L. & MEHTA, R. D. 1995*b* On using Taylor's hypothesis for three-dimensional mixing layers. *Phys. Fluids* **7**, 1516–1518.

METCALFE, R. W., ORSZAG, S. A., BRACHET, M. E., MENON, S. & RILEY, J. J. 1987 Secondary instability of a temporally growing mixing layer. *J. Fluid Mech.* **184**, 207–243.

MIYAUCHI, T., KAWANO, K. & SHINGOU, M. 1991 The coherent structure in turbulent mixing layers (structure in the core and rib regions). *Computers Fluids* **19**, 401–412.

MONKEWITZ, P. A. 1988 Subharmonic resonance, pairing and shredding in the mixing layer. *J. Fluid Mech.* **188**, 223–252.

MOSER, R. D. & ROGERS, M. M. 1991 Mixing transition and the cascade to small scales in a plane mixing layer. *Phys. Fluids* A **3**, 1128–1134.

MOSER, R. D. & ROGERS, M. M. 1993 The three-dimensional evolution of a plane mixing layer: pairing and transition to turbulence. *J. Fluid Mech.* **247**, 275–320.

NYGAARD, K. J. & GLEZER, A. 1990 Core instability of the spanwise vortices in a plane mixing layer. *Phys. Fluids* A **2**, 461–463.

NYGAARD, K. J. & GLEZER, A. 1991 Evolution of streamwise vortices and generation of small-scale motion in a plane mixing layer. *J. Fluid Mech.* **231**, 257–301.

PATNAIK, P. C., SHERMAN, F. S. & CORCOS, G. M. 1976 A numerical simulation of Kelvin-Helmholtz waves of finite amplitude. *J. Fluid Mech.* **73**, 215–240.

PIERREHUMBERT, R. T. & WIDNALL, S. E. 1982 The two- and three-dimensional instabilities of a spatially periodic shear layer. *J. Fluid Mech.* **114**, 59–82.

RILEY, J. J. & METCALFE, R. W. 1980 Direct numerical simulation of a perturbed turbulent mixing layer. *AIAA Paper* 80-0274.

ROGERS, M. M. & MOSER, R. D. 1991 The three-dimensional evolution of a plane mixing layer. Part 1. The Kelvin-Helmholtz rollup. *NASA TM* 103856.

ROGERS, M. M. & MOSER, R. D. 1992 The three-dimensional evolution of a plane mixing layer: the Kelvin-Helmholtz rollup. *J. Fluid Mech.* **243**, 183–226.

ROGERS, M. M. & MOSER, R. D. 1993 Spanwise scale selection in plane mixing layers. *J. Fluid Mech.* **247**, 321–337.

ROGERS, M. M. & MOSER, R. D. 1994 Direct simulation of a self-similar turbulent mixing layer. *Phys. Fluids* **6**, 903–923.

TOWNSEND, A. A. 1976 *Structure of Turbulent Shear Flow* (2nd Edn). Cambridge University Press.

TUNG, C. H. 1992 Initial streamwise vorticity formation in a two-stream mixing layer. PhD Dissertation, Department of Mechanical Engineering, University of Houston.

WALLACE, J. M. & FOSS, J. F. 1995 The measurement of vorticity in turbulent flows. *Ann. Rev. Fluid Mech.* **27**, 469–514.

WATMUFF, J. H. 1995 High-speed real-time processing of cross-wire data. *Expl Thermal Fluid Sci. J.* **10**, 74–85.

WINANT, C. D. & BROWAND, F. K. 1974 Vortex pairing: the mechanism of turbulent mixing layer growth at moderate Reynolds number. *J. Fluid Mech.* **63**, 237–255.

YANG, Z. & KARLSONN, S. K. F. 1991 Evolution of coherent structures in a plane shear layer. *Phys. Fluids* A **3**, 2207–2219.

ZHANG, Y. Q., HO, C. M. & MONKEWITZ, P. 1985 The mixing layer forced by fundamental and subharmonic. *IUTAM Symp. on Laminar-Turbulent Transition, Novosibirsk* (ed V. Kozlov), pp. 385–395. Springer.